Title	Precise Measurement of the Cross Section for 2.46 GeV/c π^-p Elastic Scattering at All Angles
Author(s)	Amako, Katsuya
Citation	大阪大学, 1979, 博士論文
Version Type	VoR
URL	https://hdl.handle.net/11094/27749
rights	
Note	

Precise Measurement of the Cross Section
for 2.46 GeV/c π^-p Elastic Scattering
at All Angles

Precise Measurement of the Cross Section for 2.46 GeV/c π^-p Elastic Scattering at All Angles

by

Katsuya AMAKO

February 28, 1979

ACKNOWLEDGEMENTS

I would like to thank many people without whom the present experiment could not have been completed.

First of all, I wish to express my sincere appreciation to the group leader, Professor R. Kajikawa, for his support and encouragement throughout the experiment.

I am also much grateful to Professor Y. Sumi for his excellent guidance and advice. He has undertaken a laborious task of reading the manuscripts with numerous helpful comments, suggestions and corrections.

I deeply acknowledge to Professor S. Takagi for his warm hospitality and encouragement.

I would especially like to thank Dr. T. Tsuru for his careful advices, cooperation and hardwork throughout the experiment.

The success of the experiment has entirely depended upon the devoted effort of all members of our collaboration (Nagoya-Hiroshima-Osaka-Kyoto-KEK); besides the above mentioned persons, these members are: Dr. M. Fukushima, Dr. S. Iwata, Dr. H. Kobayakawa, Mr. T. Matsui, Mr. A. Miyamoto, Dr. K. Mori, Dr. T. Nakanishi, Mr. Y. Ohashi, Dr. C.O. Pak, Mr. T. Shimomura, Dr. S.Suzuki, Mr. T. Tauchi, Dr. K. Baba, Dr. I. Endo, Mr. S. Kadota, Mr. S. Terada, Dr. T. Matsuda, Mr. Y. Takeuchi, Dr. N. Tokuda, Mr. K. Egawa and Dr. A. Tamura.

Thanks are also due to the staffs of Counter Group and Beam Channel Group at KEK for their kind supports.

Finally, I thank my wife Yoko for her invaluable support and steady encouragement during a long time to complete the present work.

ABSTRACT

The differential cross section for the $\pi^- p$ elastic scattering has been measured at an incident momentum of 2.46 GeV/c in a wide range of the momentum transfer t; $0.05 \lesssim |t| \lesssim 3.7$ $(\mathrm{GeV/c})^2$. The measurement has been made by detecting scattered pions in coincidence with recoil protons with a large aperture magnetic spectrometer placed at a forward direction and a track detector system at the other large angle side. A statistical accuracy of the present data is typically of a few to several % in almost whole range of t. Even in the worst case where the cross section reaches its minima of less than 0.02 $\mathrm{mb/(GeV/c)}^2$ the accuracy is as good as 16 %, which has not hitherto been attained by any other similar measurement.

The data show a sharp forward diffraction peak followed by a dip at $|t|=0.7$ $(\mathrm{GeV/c})^2$, a broad secondary peak, two pronounced dips at $|t|=2.5$ and 3.2 $(\mathrm{GeV/c})^2$ and a backward peak. These structures, especially those at larger values of $|t|$ are clarified all together in a quantitative way by a single experiment for the first time.

The results are compared with the existing sets of phase shift analysis. Neither of them can explain the behavior of the data in the vicinity of the last two dips. A possible existence of so-called Ericson fluctuations is also examined by using the present data. No evidence for Ericson fluctuations is found.

CONTENTS

II. EXPERIMENTAL METHOD

B. EXPERIMENTAL APPARATUS

III. DATA ANALYSIS

E. IDENTIFICATION OF ELASTIC EVENTS

IV. CALCULATION OF THE CROSS SECTION

I. INTRODUCTION

The pion-nucleon elastic scattering is one of the most fundamental processes to study the hadron-hadron interactions, and for this reason a large amount of effort has so far been made both experimentally and theoretically. Below 2 GeV/c of the pion laboratory momentum p_L, the existing experiments for differential cross section as well as polarization cover almost all momenta and scattering angles.[1) On the other hand, there are four sets of phase shift analysis in this energy region; those by CERN,[2) Saclay,[3) Karlsruhe-Helsinki[4) and CMU-LBL.[5) These analyses have confirmed many resonances in the pion-nucleon system which have been served as a main basis for theoretical understanding of the baryon spectroscopy in terms of the quark models. As a result, one may say that in this energy region essential features of the pion-nucleon elastic processes have now been well clarified and some discrepancies among different analyses are rather minor ones.

Above 2 GeV/c, however, a difficulty of performing an exact phase shift analysis, together with a lack of experimental data with high quality particularly for the π^-p elastic and charge exchange scattering, prevent us from making a further detailed analysis of the processes. The situation is especially severe at large angles where the cross section becomes drastically small.

Recently, there has been a great deal of interest in furthering our understanding of hadron spectroscopy above 2 GeV/c because it is very important to know if various strong interaction models are adequately operative or not in this regime. These models are for example, the $SU(6)\otimes O(3)$ quark model,6) the dual string model,7) the various bag models8) and dual resonance models.[9] From this point of view, several authors have proposed phenomenological models for the pion-nucleon elastic amplitudes above 2 GeV/c. For examples, using a dual interference model Ma and Shaw have found the higher resonance states.[10] On the other hand, using an impact-parameter type representation for the amplitudes Hendry has performed the partial wave analysis up to 10 GeV/c,[11] while on the basis of dispersion relation the Karlsruhe-Helsinki group has given another result of partial wave analysis using the data up to 6 GeV/c.[12] To give further clues for these analyses, it is important to supply a good deal of systematic data at p_L>2GeV/c over as wide angular range as possible.

Another set of pion-nucleon elastic amplitudes is given by the Regge-pole model[13] which may be applicable in a range of energies sufficiently higher than those in the resonance region. In the conventional Regge-pole model the diffractive part of the amplitudes is given by the exchange of the Pomeron, while the peripheral part is assumed to be an appropriate superposition of various meson-pole exchanges. This model has successfully explained the behavior of the cross section and polarization in the forward angle region.[14] In the backward angle region, however, this model cannot explain the behavior of the polarization data.

Meanwhile, the duality scheme has been proposed. In this model the resonance contribution at low energies is related to the Regge-pole exchange at high energies through the finite energy sum rule.[15] With the duality concepts, the dual interference model has been successfully applied to confirm resonances above 2 GeV.[10]

Recently, Hara, Kuroda and Takaiwa have proposed a peripheral orbit model,[16] in which an incoming hadron is assumed to revolve on a peripheral orbit around a target hadron when they make a collision at high energies.

This model provides both the real and imaginary parts of the various reaction amplitudes at all angles in a wide range of energies.$^{17)}$

In the vicinity of 5 GeV/c, Schmidt et al.$^{18)}$ have reported that a considerable fluctuation in the differential cross section for large angle π^+p elastic scattering is observed for a small difference in the incident momentum of only 80 MeV/c. This fluctuation may be interpreted as a possible evidence for the Ericson fluctuation.$^{19)}$ Schmidt et al. have found that their π^-p elastic scattering data are consistent with no fluctuations over the whole t-range. However, they have noted that there is some indication of fluctuations for $-t \gtrsim 5$ $(\mathrm{GeV/c})^2$ and that their data cannot rule out fluctuations in π^-p; the π^-p differential cross sections in question are in general considerably smaller than those for the π^+p. The smallness of the fluctuation in π^-p elastic scattering at this momentum may be accounted for by a fact that the density of resonance states is much larger for the π^-p elastic scattering than for the π^+p one. With this respect it may be expected that the fluctuation is observed at momenta lower than 5 GeV/c for the π^-p elastic scattering.

The present experiment is aimed at measuring differential cross sections over almost all angles for the π^-p elastic scattering in a momentum range between 2.1 and 3.5 GeV/c to provide foundamental data for further understanding of the process in this energy region. The present paper deals with the measurement at 2.46 GeV/c.

In Section II we describe the experimental method. In Section III and Section IV we discuss the methods and procedures employed in the data analysis and the cross section calculation. Finally, we give the results obtained and related discussions in Section V.

II. EXPERIMENTAL METHOD

A. GENERAL DESCRIPTION

The $\pi^- p$ elastic scattering is a kinematically simple process, because the reaction is described by two independent variables, being taken, for instance, the incoming momentum and the laboratory scattering angle. Experimentally, however, this does not mean that it is enough to measure these variables only, since there are significant backgrounds from other inelastic processes. In $\pi^- p$ interactions, the total cross section σ_t is $\sim$ 33 mb at the beam momentum of 2.5 GeV/c, while the elastic one σ_{el} is $\sim$ 7 mb. Accordingly, one must discriminate an elastic event without any ambiguity from five times greater background ones. The situation is more serious when one goes to the large angle region where the elastic differential cross section becomes drastically small.

Therefore, we require the following conditions for observed events to distinguish the elastic process from the backgrounds:

i) The momentum vectors of the two particles in the final states are coplanar.

ii) The angle between them must lie in a range which is determined by the elastic pion-nucleon kinematics.

iii) The momentum of the forward going particle, which is determined by a magnetic spectrometer, must have a value calculated by the elastic kinematics.

In order to select the elastic events in this manner, we must measure the momentum of forward going particle and the angles of both forward and backward going particles.

A schematic drawing of the equipment layout which has been adopted in the experiment is shown in Fig. 1. The beam was defined by five scintillation counters and a gas Cherenkov counter. The direction of the beam was determined by six planes of multiwire proportional chamber. The beam momentum was tagged by a momentum hodoscope which had ten scintillation counters.

The direction and magnitude of the momentum of the forward going particle were measured by the magnetic spectrometer which consisted of a large aperture magnet (TOKIWA) and thirty-six planes of wire spark chamber (C1 - C4). The spectrometer covered almost whole range of the scattering angle, while the cross section varied drastically with angle, so that an efficient detection had to be made particularly in a smaller cross-section region. This was realized by dividing the acceptance of the spectrometer into several different regions using three scintillation hodoscopes (T1 - T3). The direction of the backward going particle was determined by twelve planes of wire spark chamber (C5 - C6). A scintillation counter (T4) and a scintillation hodoscope (T5) provided the trigger signal of the wire spark chambers for the backward going particles. A lucite Cherenkov counter (LC) was used to distinguish pions from protons in the backward arm.

As described above, the inelastic processes became severe noises in selecting the elastic event in the large angle region. To reduce these noises, veto counters (A1 - A2) were attached to the target assembly, which rejected a considerable part of inelastic events which contained additional $\pi^{\pm}$ or π°.

B. EXPERIMENTAL APPARATUS

1. BEAM

The π^- beam was produced at an internal target of the 12 GeV proton synchrotron at National Laboratory for High Energy Physics, KEK. The internal target was an L-shape beryllium of 1 mm diameter and 15 mm length. The production angle of the beam was 10° with respect to the tangent of circulating protons. A schematic layout of the beam line is shown in Fig. 2a and 2b.

The first stage of the line consisted of horizontal and vertical beam slits, two quadrupole and bending magnets, and an overlapping type scintillation hodoscope. The hodoscope was set at the first focus point FO of the beam. The hodoscope had eight 9 mm (width) × 50 mm (height) and two 6 mm (width) × 50 mm (height) scintillators, and these were overlapped in 3 mm interval so that the momentum of the beam was divided into nineteen bins. The momentum dispersion at FO was 12.0 mm per $\Delta p/p = 1.0$ %.

The second stage of the line consisted of two quadrupole magnets, three bending magnets and a vertical steering magnet. The beam was steered and refocused achromatically to the center of the hydrogen target after this stage. Vacuum pipes were utilized to avoid multiple scattering of the beam.

A beam survey around the target point was performed. The optimum strength for each magnet was determined at several energy points by measuring the intensity and the profile of the beam. Six planes of multiwire proportional chambers were used to monitored the beam profile.

The proton synchrotron was operated at 8 GeV throughout the experiment and the beam intensity was $1 \sim 2 \times 10^5$ π^- per burst with relative momentum acceptance of ± 1.0 % at 2.46 GeV/c. The beam spill time was 350 ms in every cycle of 2 s.

2. BEAM PROPORTIONAL CHAMBERS

2.1 General

There were three sets of multiwire proportional chamber (MWPC) in the beam line. Each set of the chamber had two sensitive planes. A direction of the incident pions was measured event by event using these chambers. The chambers were also the powerful monitor in tuning the beam line elements. The careful design consideration was made and a good performance had to be attained because the chambers were operated in the high intensity beam. The dimension of the chambers is shown in Table 1.

2.2 Construction

The exploded view of the chamber is shown in Fig. 3. The chamber frame was made of epoxy of 5 mm thick. There were five planes of electrodes: two of them were anode wire planes, the others cathode planes. The two anode planes had vertical wires determining the x-coordinate and horizontal wires for the y-coordinate.

The anode planes had wires of gold-plated tungsten, 20μ in diameter and spaced at 2 mm intervals, while the cathode planes were aluminized mylar sheets of 12μ thick. Two sheets of 50μ thick mylar foils were stretched at the front and the back of the chamber so as to make the required enclosure for the gas circulation.

2.3 Gas system

The gas used through the experiment was a mixture of 75.0 % argon, 24.5 % isobutane and 0.5 % freon-13b1. As well known$^{20)}$, this mixture gas induces the degradation of the chamber in a high intensity flux of charged particles. To reduce this effect, 7.0 % of methylal was added to the above gas mixture, which was supplied from an automatically controlled gas mixing system. Among the ingredients of the mixture gas, freon captures ionized electrons in the chamber, so that an instability of its mixing ratio induces an inefficiency of the chamber. A method adopted to control the mixing ratio of the gas is the so-called pressure control method in which the mixing ratio is determined by monitoring and controlling the partial pressure of each gas. To control a small mixing ratio accurately, this method is more adequate than the so-called volume control method in which the mixing ratio is determined by controlling the flow rate of each gas using flowmeters.

2.4. Electronics

The KEK standard readout system[21)] was used to readout chamber signals. In this system, a signal from the chamber was encoded as follows:

i) A raw signal was amplified by a factor of six by a pre-amplifier mounted on each chamber.

ii) The push-pull signal from the pre-amplifier was transmitted through a 40 m long twisted pair cable to the counting room.

iii) The signal was received by a comparator and amplified up to the TTL logic level, and stored into a flip-flop which was gated by a strobe signal from the trigger counters. These circuits were mounted in a single span CAMAC module (MEMORY MODULE) in which signals from sixteen wires could be treated at the same time.

iv) An ENCODER MODULE selected hitted flip-flops and encoded their addresses.

v) The encoded addresses were stored in a BUFFER MEMORY MODULE for a further processing by an on-line computer.

The ENCODER and the BUFFER MEMORY MODULE were both CAMAC standard modules. The threshold of the system was 1.5 mV for a 1.8 kΩ load-resistance at the input of the pre-amplifier.

2.5 Performance

The optimum operating voltage of the chambers was found to be 4.0 to 4.2 kV. Fig. 4 shows the high voltage curve of the chambers. The efficiency of each chamber was around 95 % for the beam intensity of $\sim 10^5$ particles per burst, whereas the same chamber showed 99.9 % when a radio active source was used. The dead time of the readout system accounted for this disagreement. The gate time used in the experiment was 150 ns.

The leakage current of the high voltage of the chamber was monitored using a current meter. The leakage of every chamber was less than 1 μA at the end of the beam spill time and all chambers showed no degradation of the detection efficiency.

3. TARGET

The liquid hydrogen target consisted of a cylinder, 613 mm long and 40 mm in diameter, with mylar walls of 180μ thick. An aluminum jacket of cylinder of 88 mm in diameter and 1 mm thick provided a necessary vacuum insulation. The beam windows at both ends of the vacuum insulation were mylar sheets of 180μ thick. In Fig. 5, a cross sectional view of the target is shown together with veto counters. A cryogenic system was a closed circuit helium refrigeration system, Cryodyne Model 1023, which consisted of a 3 HP compressor and two-stage refrigerator of Gifford McMahon cycle. A purified hydrogen gas from a reservoir tank was liquified in a condenser and flowed into the target cylinder. The cooling power of the refrigerator was about 10 watts at 20°K. A quick filling or evacuation of the liquid hydrogen was achieved only by handling a cryovalve which controlled the path of evapolated gas from the liquid hydrogen target. The time needed to evacuate the hydrogen was about five minutes. The liquid hydrogen level in the target was continuously monitored by measuring the change of carbon resisters attached to the target cylinder.

4. SPECTROMETER MAGNET

A large aperture spectrometer magnet called TOKIWA was used to measure momenta of forward going particles. The charge state of the particles was also determined from the curvature of the trajectory in the magnetic field. The magnet had an aperture of 2200 mm width, 500 mm height and 750 mm length. Since the field distribution of such a wide aperture magnet was expected to be strongly non-uniform, a precise field measurement was performed on a dense three dimensional grid. Among various methods to determine the magnetic field distribution, a method using a Hall generator was chosen for its mechanical simplicity. A main difficulty to use the Hall generator in a measurement of such a non-uniform field was the effect due to the field component parallel to the Hall plate. By a simultaneous measurement of three field components at a given spatial point and a careful correction to the effect of the parallel field component to the Hall plate, the field distributionin the effective volume of the magnet was determined with an accuracy of 32 G.[22) The measurement was performed by an automatically controlled field measuring machine. The total number of mesh points was amounted to 3×10^4. The measured data were compiled into the field distribution on the 50 mm × 50 mm × 50 mm mesh points and stored into a disk of an off-line computer.

The current of the magnet was set at 4200 A throughout the experiment except for the check run of the acceptance of the spectrometer. The field integral for a central orbit was $\int B\,dl = 11.4$ kG·m. The field of the magnet was monitored using the NMR probe attached at the pole surface of the magnet. The current of the magnet was also checked in each time interval between beam spills.

5. COUNTERS

5.1. General

A counter system of the spectrometer consisted of scintillation counters and Cherenkov counters. Main functions of the counter system were to define the acceptance of the spectrometer and to provide the trigger signal of an elastic candidate event for the wire spark chamber system. To suppress trigger signals from inelastic proccesses, the off-acceptance region of the spectrometer was covered by veto counters as much as possible. A rough check for the correlation of the forward and backward going particles was done by the counter system to enrich elastic events. The multiplicity of charged paticles was also measured to suppress inelastic processes. A perspective view of the counter system is shown in Fig. 6.

5.2. Beam counters

There were five scintillation counters B1, B2, B3, BA1 and BA2 in the beam line. A threshold type gas Cherenkov counter was also set in the beam line to separate pions from other charged leptons.

The veto counters BA1 and BA2 had a hole of 35 mm and 20 mm in diameter, respectively, at the center of effective area, to cut the beam halo.

The gas Cherenkov counter had an acceptance for the beam whose diameter was as large as 13 mm and angular divergence of up to 10 mrad. A gas used in the counter was Freon-12. The effective path length of the Cherenkov radiator was 80 cm. A signal from the Cherenkov counter was not included in the event trigger logic but read by an ADC and its pulse height was recorded.

5.3. Veto counters

There were three veto counters A0, A1 and A2. A0 was set in the beam line at the downstream of the hydrogen target to veto against unscattered beam particles and particles which were scattered in an extremely forward direction.

As discussed in II-A, since the inelastic processes became serious backgrounds, particularly in the large angle region, A1 and A2 were attached to the target assembly to reject a considerable part of events which produced $\pi^{\pm}$ or π° inelastically. Each of the veto counters consisted of two layers of scintillator of 10 mm thick and a lead plate of 6 mm thick between the scintillators.

5.4. T1 hodoscope

This hodoscope had two functions: i) To separate a large angle scattered event from forward and backward scattered events. ii) To select an event which roughly satisfied the coplanarity. The hodoscope consisted of three scintillation counters; T1-0, T1-1 and T1-2. T1-0 covered the forward angle region $\Theta_{lab} = 0 \sim 8°$. The remaining large angle region was horizontally divided into two regions which were covered by T1-1 and T1-2, respectively. The selection of an event which was likely coplanar was performed by combining the signal from T1-1 and T1-2 with the signal from T-5 hodoscope whose acceptance was also vertically divided into two regions. The dimension of the hodoscope is shown in Table 2.

5.5. T2 hodoscope

This hodoscope consisted of vertically segmented eight scintillation counters: T2-1 to T2-8. The bin width of the counters was different between forward and large angle regions because scattered particles were likely to concentrate in the forward direction. The dimension of the hodoscope is shown in Table 2.

A main function of T-2 was to separate the acceptance of the spectrometer into several regions to detect the large angle event efficiently. In the most measurements, the signals from T2-1 to T2-4 were combined to cover the forward angle region, T2-5 and T2-6 were combined to cover the medium angle region, and T2-7 and T2-8 were combined to cover the large angle region. These combinations were sometimes modified according to a condition of measurements.

The charged multiplicity of events was also measured by this hodoscope to suppress triggers due to inelastic processes.

5.6. T3 hodoscope

This hodoscope consisted of thirteen scintillation counters. The dimension of the hodoscope is shown in Table 2. An essential function of T3 was to confirm whether a scattered particle went through the forward arm of the spectrometer. Except for the measurement in the backward angle region, all the signals from these thirteen counters were added.

For the measurement of the backward cross section, T3 played a different role. Since the backward cross section was about three order of magnitude smaller than the forward one, it was difficult to obtain sufficient numbers of trigger of the backward scattered events without an appropriate reduction of the event rate for the forward scattered ones. This reduction of forward events was realized by using the fact that the forward going pion and proton have different trajectories in the spectrometer: the forward pion or proton struck a different bin of T3 hodoscope.

By grouping the signals from T3 and combining with appropriate signals from T2 and T5 hodoscopes, the efficient discrimination of the backward scattered event from the forward one was achieved.

The time-of-flight between B3 and T3 was served for the particle identification for the forward going particles.

5.7. T4 counter

This was scintillation counter of single plate set near the hydrogen target. The function of this counter was to reject backward going particles which came from other origins than the target. The dimension of T4 is shown in Table 2.

5.8. T5 hodoscope

This consisted of totally twelve scintillation counters being arranged vertically in two divisions and horizontally in six divisions. The dimention of T5 is shown in Table 2.

The functions of this hodoscope were as follows: (i) To select an event which was likely coplanar by combining the signals from T1. (ii) To determine whether the event satisfied roughly the elastic kinematics or not, incorporating with the signals from T2 and T3. (iii) To measure a charged-multiplicity of backward scattered particles.

The time-of-flight between B3 and T5 was measured for the particle identification of backward going particles. The pulseheight of this hodoscope was also measured by ADCs event by event.

5.9. Lucite Cherenkov hodoscope

This hodoscope consisted of five threshold type lucite Cherenkov counters. The dimension of the hodoscope is shown in Table 2. The function was to reject the backward scattered protons with the velocity less than $\beta \sim 0.7$ and thus to enrich the elastic events in which the pions were backward scattered with much greater velocity than 0.7.

6. TRIGGER LOGIC

6.1. Basic logic

Criteria for the event selection should have been changed from one measurement to another because the background noises, the counting rate and the kinematical conditions varied with the incident momentum of the beam, so that, the logic circuits had to be as flexible as possible.

In constructing trigger signals there were four categories of signal combination which was served as the basic logic.

i) Beam logic

There were six types of signal combination to identify incident particles:

$\mathrm{BEAM0} = \mathrm{B1} * \mathrm{B2} * \mathrm{B3},$

$\mathrm{BEAM1} = \mathrm{BEAM0} * \overline{\mathrm{BA1}} * \overline{\mathrm{BA2}},$

$\mathrm{BEAM2} = \mathrm{BEAM1} * (\ \overline{\text{100 ns dead time}}\ ),$

$\mathrm{BEAM3} = \mathrm{BEAM2} * (\ \overline{\text{nearby particle}}\ ),$

$\mathrm{BEAM4} = \mathrm{BEAM3} * (\ \overline{\text{WSC dead time}}\ ) * (\ \overline{\text{computer busy}}\ ),$

$\mathrm{BEAM5} = \mathrm{BEAM3} * \mathrm{GC}\ .$

BEAM0 defined beam particles while BEAM1 selected particles which passed through the two hole counters among them. BEAM2 was obtained by vetoing BEAM1 for 100 ns after the passage of beam particles. This dead time was due to the recovery time of the trigger logic system. BEAM3 rejected the beam particles which had a chronologically near-by particle within 25 ns. This time was due to the time resolution of the trigger logic system. BEAM4 was the final definition of the beam particle including the dead time of the wire spark chamber system and the acquisition time of the on-line computer. BEAM5 picked up the particles which triggered the gas Cherenkov counter among particles of BEAM3.

ii) Forward arm logic

There were five kinds of signal combination to define a forward going particle. These were obtained by grouping the T2 hodoscope into several combinations:

$$F0 = BEAM3 * \sum_{all} T1 * \sum_{all} T2 * \sum_{all} T3 ,$$

$$F1 = BEAM3 * \sum_{all} T1 * \sum_{1}^{4} T2 * \sum_{all} T3 ,$$

$$F2 = BEAM3 * \sum_{all} T1 * \sum_{5}^{6} T2 * \sum_{all} T3 ,$$

$$F3 = BEAM3 * \sum_{all} T1 * \sum_{7}^{8} T2 * \sum_{all} T3 ,$$

$$F4 = BEAM3 * \sum_{all} T1 * \sum_{some} T2 * \sum_{some} T3 .$$

F0 covered the whole acceptance of the forward arm. This signal was mainly used for the check of the forward wire spark chambers. F1, F2 and F3 covered the forward, the intermediate, and the large angle regions, respectively. F4 separated out the forward going proton event from the forward going pion one using the difference in trajectories for these particles in the magnetic field. The combinations of the T2 and T3 hodoscopes were prepared from the results of a Monte-Carlo simulation.

iii) Backward arm logic

There were five kinds of signal combination to define backward going particles:

$$B1 = BEAM3 * T4 * \sum_{all} T1 * \sum_{all} T5 ,$$

$$B2 = BEAM3 * T4 * \sum_{all} T1 * \sum_{9}^{12} T5 ,$$

$$B3 = BEAM3 * T4 * [(T1{-}1) * \sum_{odd} T5 + (T1{-}2) * \sum_{even} T5] ,$$

$$B4 = BEAM3 * T4 * \sum_{all} T1 * \sum_{some} T5 ,$$

$$B5 = B2 * LC .$$

B1 covered the whole angular region of the backward arm. As seen in Fig. 6, T5-9 to T5-12 mainly covered the backward region, so B2 was used to trigger backward events. B3 selected the event which was likely coplanar. As described in 6.1 -(ii), B4 separated out the backward event from the forward one incorporating with F4 signal. B5 also enriched the backward event using the lucite Cherenkov counter which rejected slow particles.

iv) Veto signal

The standard definition of the veto signal was:

$$ANTI = A0 * A1 * A2 * MA1 * MA2 ,$$

where MA1 and MA2 were signals from the multiplicity logic units. MA1 was set when T2 detected more than two charged particles, while MA2 was when T3 hodoscope did.

6.2. Trigger logic

Trigger signals to fire the wire spark chamber system for a candidate of the elastic event were constructed from appropriate combinations of the basic logic signals described in 6.1. There were six types of the trigger signals:

$$\mathrm{EV1} = \mathrm{F1} * \mathrm{B1} * \overline{\mathrm{ANTI}}\ ,$$

$$\mathrm{EV2} = \mathrm{F2} * \mathrm{B3} * \overline{\mathrm{ANTI}}\ ,$$

$$\mathrm{EV3} = \mathrm{F3} * \mathrm{B2} * \overline{\mathrm{ANTI}}\ ,$$

$$\mathrm{EV4} = \mathrm{F1} * \mathrm{B2} * \overline{\mathrm{ANTI}}\ ,$$

$$\mathrm{EV5} = \mathrm{F1} * \mathrm{B5} * \overline{\mathrm{ANTI}}\ ,$$

$$\mathrm{EV6} = \mathrm{F4} * \mathrm{B4} * \overline{\mathrm{ANTI}}\ .$$

EV1, EV2 and EV3 had acceptances for the forward, intermediate and large angle scattered particles, respectively.

EV1 included both from forward scattered pions and protons. Therefore, EV1 covered forward and backward cross section regions simultaneously. In practice, however, the detection of events from the backward cross section region was heavily masked by events for the forward cross section which is larger by three orders of magnitude than the backward one. The efficient detection of events for the backward cross section was performed by EV4, EV5 and EV6.

EV4 had larger acceptance for the event of the backward cross section, but it inevitably included forward events because of a finite geometry of the hydrogen target. EV5 included the signal from the lucite Cherenkov counter. The most efficient trigger signal for the measurement of the backward cross section was EV6. In this trigger signal, as described in 6.1.-ii), the backward events were perfectly discriminated from the forward ones using the difference in their trajectary in the magnetic field.

The final trigger signal was the logical OR of all the trigger signals described above. In the experiment, the cross sections at the forward angles and the backward ones were measured independently. Therefore, there were two final trigger signals:

$$\mathrm{FORWARD} = \mathrm{EV1} * 1/\mathrm{CND1} + \mathrm{EV2} * 1/\mathrm{CND2} + \mathrm{EV3}\ ,$$

$$\mathrm{BACKWARD} = \mathrm{EV4} + \mathrm{EV5} + \mathrm{EV6},$$

where EV1 and EV2 were reduced to 1/CND1 and 1/CND2, respectively, to enrich EV3 signal.

7. SPARK CHAMBERS[23)]

7.1. General

The spectrometer system had to cover the whole angle of π^-p elastic scattering process at the same time, and track detectors with a large effective area were needed. Wire spark chambers (WSC) were adopted as a central track detector in the spectrometer system because of its relative easiness in achieving a large detection area with rather low cost of a readout system per wire. There were totally fourty-eight planes of WSC and the dimension of these chambers are listed in Table 3.

7.2. Construction

In Fig. 7, the exploded view of the chamber is shown. The chamber frames were made of a fiberglass-epoxy bond (G-10) of 10 mm thick. The electrodes were made of a copper wire of a diameter 0.12 mm with a spacing of 1 mm. The directions of wires of two electrodes planes were parallel in chambers C1 and C2, while made an angle of 30° in C3 to C6. The main difficulties in constructing larger chambers were how to fasten the wire planes to the chamber frame and how to support the chamber frame rigidly against the tension force of the wires. A method adopted to set the wire planes onto the frame was as follows:

i) The wires were first wound with 1 mm spacing around an octagonal shaped winding frame whose circumference was larger than the size of the chamber frame on which the wires were to be fastened.

ii) The wires were glued onto a support bar fixed on the widing frame.

iii) The wire plane was then expanded and streched with a tension of 150 g per wire using a wire streching machine.

iv) The chamber frame which was strained previously to compensate the tension force of the wires, was set just under the wire plane.

v) The wire plane was glued onto the chamber frame using epoxy bond. A mylar sheet of 0.05 mm was used for a gas window of the chamber. The mylar window at the electrically positive side of the wire plane was coated with an aluminium foil which was also used as the electrode for the clearing field.

7.3. High voltage

In order to obtain an uniform detection efficiency, the high voltage pulse had to be distributed uniformly over the entire chamber area. This was accomplished by feeding a high voltage square pulse at three different points on the wire plane. The high voltage square pulse of 20 ns rise time and 200 ns width was obtained as follows: Co-axial cables with 20Ω impedance were charged up by a high voltage power supply, then discharged by a thyratron trigger. The pulse was transmitted through another 20Ω impedance co-axial cable whose end at the chamber side was terminated through a 20Ω carbon resister. The maximum repetition rate of the high voltage system was 50 Hz.

7.4. Gas

A gas mixture used in the experiment was composed of 70.0 % Neon and 30.0 % Helium. The gas was once stored in a buffer tank and then distributed to each chamber. The flow rate of the gas at both inlet and outlet of the chamber was monitored by flowmeters.

7.5. Readout system

A magnetostrictive delay line was used to read out spark positions of the wire chambers. The magnetostrictive line has such a property that when a magnetic field induced by a current due to a spark in a nearby wire is impressed on a part of the line, an acoustic wave is induced at that part and is propagated along the line. A spark position was determined by measuring a time difference between the arrivals of acoustic waves induced, respectively, by the sparked wire and by a fiducial wire which was set at an appropriate position.

Before setting the magnetostrictive delay line to the chamber, the line was permanently magnetized longitudinally. The delay line was covered by a teflon tube and laid down on the electrode wires. A mylar tape of 0.05 mm thick was inserted between the delay line and the electrode for an electric insulation. For the chambers having large effective area, the attenuation of the acoustic wave was a serious problem. To overcome this difficulty, a strip of an aluminum foil was attached over the delay line. The pulse height of the acoustic wave was almost doubled by this foil. A pickup coil was set at the end of the magnetostrictive line. This coil was mounted in a cylindrical permanent magnet of 140 Gauss which produces a bias magnetic field around the coil. It was essentially important to shield the delay line from stray external magnetic fields of the spectrometer magnet since an appreciable field along the line would disturb the magnetization direction of the line, thereby much attenuating the acoustic wave amplitudes. Iron plates of 9 mm thick were therefore used as magnetic shields for delay lines which were set close to the fringe field of the spectrometer magnet.

The signal of 2 $\sim$ 4 mV in pulse height from the pickup coil was transferred through a co-axial cable of 3 $\sim$ 10 m long to a pre-amplifier which was set at the experimental hall. The gain of the pre-amplifier was about 500. The signal was again transferred through a 20 m co-axial cable to a zero-cross discriminator.

The KEK standard of the readout system[24)] was used for further processing of the signal. The system consisted of a WSC controller, a clock generator and an interval scalar, all of them being of CAMAC standard. The clock generator provided a clock pulse of 20 MHz to the interval scalar. The front fiducial signal started the interval scalar and signals from the sparked wire and the back fiducial stopped the scalar. The WSC controller generated an interrupt signal to a computer when spark positions were encoded by the system.

7.6. Performance

The local position dependence of the detection efficiency of a large size chambers was checked using a radioactive source. This was carried out as follows: the effective area of the chamber was divided by eight different regions, the supplied high voltage dependence of the detection efficiency in each sub-divided region was measured. In Table 4, the high voltage values <m> where the efficiency at each area reaches 50 % are listed. As seen in the table, the deviations of m from the mean value <m> at each area were less than 8 %.

In Fig. 8, a typical example of the supplied high voltage dependence of the detection efficiency for the 3 m × 0.8 m chamber is shown. In Fig. 9, a typical example of the delay time and the clearing field dependence of the detection efficiency for the same chamber is shown. The efficiency of the chamber reached 99 % at the high voltage of 9 kV for the single track. The memory time was 600 ns for the clearing field of 70 V.

8. DATA ACQUISITION SYSTEM

8.1. Data acquisition hardware

A data acqusition system consisted of a CAMAC standard system for relevant electronics, a BDO-11 branch driver and a PDP11/45 computer. A schematic diagram of the system is shown in Fig. 10.

There were five crates in the CAMAC system. The CAMAC modules were grouped according to their functions and were allocated to each crate. Crate No.1 was allocated to CAMAC blind scalars and a CAMAC interface module for NIM scalars. Crate No.2 was allocated to modules for the multiwire proportional chambers, bit registers, ADC modules, TDC modules and a LAM grader. The bit registers stored hitted position of the trigger counters. The ADC modules measured pulse height values of the signals from the T4 counters, the lucite Cherenkov counters and the beam gas Cherenkov counter. The TDC modules measured a time difference between two trigger signals from T3 and T5. The modules for the readout of the wire spark chambers were allocated to crates No.3 and No.4. Crate No.5 was allocated to a digital voltmeter interface which measured the current of TOKIWA and ADC modules which monitored high voltage values of all scintillation counters used in the spectrometer system.

The on-line computer was a PDP11/45 with 28 kilowords memory. The computer was linked to the CAMAC system via the BDO-11 branch driver. It was also linked to a disk drive, an 800 BPI magnetic tape drive, a keyboard and a Sony-Tektronix 4010 storage scope. The on-line computer was characterized by its ability to communicate with the outer side in a real time by means of priority and non-priority interrupts. When an interrupt was given, the computer stopped any task which it was doing and proceeded to do a task which was demanded by the interrupt.

There were five interrupt signals from the CAMAC. Flat-top-begin (FTB) and flat-top-end (FTE) interrrupts informed to the computer a time when a flat-top period of the acceleration cycle started and finished, respectively. Event interrupt (EVENT) was generated when an event which satisfied the required trigger condition occurred. Two other interrrupt signals were generated when the spark chamber readout system and the multiwire proportional chamber readout system finished their data acquisitions.

8.2. Data acquisition software

The on-line software had the following functions:

i) To control the data acquisition.

ii) To monitor the spectrometer system.

The monitor program ran as the background program, while the data acquisition program operated at the interrupt level.

The sequence of data collection by the data acquisition program was as follows:

i) When a FTB interrupt was accepted, the CAMAC system was cleared and a flag for the FTB was set. Then, the computer returned to the background job and was waiting an EVENT interrupt.

ii) When the EVENT interrupt was generated, the computer checked the status of the FTB flag and if it was on, all of signals from the trigger counter system were read and stored into the temporary buffer, and the computer returned to the background job.

iii) Interrupts from the multiwire proportional chamber system and the wire spark chamber system were generated when each system completed the data acquisition. After storing these data into the buffer area, the computer returned to the background job to wait for an other EVENT interrupt.

iv) When a FTE interrupt occurred, the CAMAC scalars were read, then all data in a beam burst stored at the buffer area were dumped onto a magnetic tape. Data of each event consisted of 256 words and the data format is shown in Fig. 11.

The monitoring program made a check of the performance of each element of the spectrometer system. The counters were monitored by checking the multiplicity and the hitted position distribution of each hodoscope. To check the multiwire proportional chambers and the wire spark chambers the multiplicity, the hitted position distribution and the detection efficiency were monitored for each chamber. The monitored results were stored in a form of histogram. The overall monitoring of the spectrometer system was performed by displaying the particle tracks of the every first event which took place during the beam burst.

The Sony-Tektronix 4010 usually displayed the particle tracks. The histograms of monitored results could be selectively displayed by keying an appropriate command from the key-board. In Fig. 12, a typical example of the particle tracks displayed on the Sony-Tektronix 4010 is shown.

The further analysis of collected data was performed at the KEK central computer HITAC 8800 by a bicycle on-line program.

III. DATA ANALYSIS

A. GENERAL PROCEDURE

The task of the data analysis is devided into two stages. The first stage consists of the reconstruction of particle tracks which determine the momentum vector of the forward going particle and the direction of the backward going one. The second stage is to select the elastic events using the results from the first stage.

The outline of the procedure taken in the first stage is as follows:

i) First, the hitted positions on the trigger counters are determined.

ii) By taking into account these position data, the track reconstruction is performed from recorded positions in all of the spark chambers at each arm.

iii) Using the above tracks before and after the spectrometer magnet, the momentum reconstruction is performed, together with the determination of the charge state of the forward going particle.

iv) The interaction vertex is determined.

v) Under the assumption that recorded events are all elastic, the coplanarity and angular correlation of the forward and backward going particles are calculated from the scattering angle of the forward going particle. The difference between the predicted value of the momentum for the forward going particle and the measured one is also calculated.

Results of the first stage were stored event by event into data summary tapes. The second stage of the analysis was performed by processing the data summary tapes.

B. RECONSTRUCTION OF TRACKS[25)]

An accurate alignment of wire spark chambers in the forward and backward arms of the spectrometer is essential to reconstruct the particle track. For this we used two sets of multiwire proportional chamber which had the same mechanical structure as described in Chapter II. Each set of the proportional chamber was aligned using a telescope before C1 and behind C3 on the central line of the forward arm. When the field of the spectrometer magnet was turned off, straight tracks which were determined by these proportional chambers defined reference lines to align the wire spark chambers in the forward arm. The spark chambers in the backward arm were aligned so that the sparks by the backward scattered particle lied on the straight line.

The procedure employed in the reconstruction of a particle track in the forward arm is as follows:

i) From the knowledge of hitted positions of T2 and T3 hodoscopes, sparks located in the acceptance of the hitted hodoscope bin are selected out.
ii) Since the straight tracks before and after the magnet must be connected smoothly, possible combinations of all sparks in the forward spark chambers are χ^2-fitted by assuming the most general form of quadratic curve.
iii) Using the combination of sparks which give the smallest value of χ^2, tracks before and after the magnet are again fitted by straight lines.

In comparison with the track finding procedure in the forward arm, that adopted in the backward arm is simple because there is no magnetic field. The procedure used in the backward arm is as follows:

i) From the knowledge of hitted position of T5 hodoscope, sparks located in the acceptance of the hitted hodoscope bin are selected out.

ii) From possible combinations of these selected sparks, a number of straight lines are obtained. Among them, the one which gives a minimum χ^2 is assumed to be the track in question.

C. DETERMINATION OF MOMENTUM

The momentum of a forward going particle was determined from the reconstructed trajectories before and after the spectrometer magnet, by using an iterative tracking method.

A computer program used for this purpose was originally developed at CERN[26)], and was slightly modified according to our experimental situation. A principle adopted in the program is as follows:

The Lorentz equation of motion for a charged particle with velocity $\vec{v}$ in a magnetic field $\vec{B}$ is

$$\vec{F} = \frac{e}{c} \vec{v} \times \vec{B} .$$

This may be re-arranged into the following two equations.[26)]

$$\frac{c}{e} p x'' = (1 + x'^2 + y'^2)^{\frac{1}{2}} [x'y'B_x - (1 + x'^2) B_y + y'B_z] ,$$

$$\frac{c}{e} p y'' = (1 + x'^2 + y'^2)^{\frac{1}{2}} [(1 + y'^2) B_x - x'y'B_y - x'B_z] ,$$

where x'' is d^2x/dz^2, etc., and p is the momentum of the particle. The coordinate system used in the expression is shown in Fig. 13.

The lowest estimate of a momentum p from which the iteration is started is determined from a bend in the path of the particle in the effective edge approximation for the magnet. Then, the above equations are solved numerically with a Runge-Kutta method using the reconstructed trajectory before the magnet and the lowest estimate for p, giving a calculated trajectory after the magnet. The calculated trajectory is compared with the observed one and the estimated momentum is now modified to give a better trajectory. Starting this modified value, the equations of motion are again solved. This loop is stopped when the calculated trajectory coincides with the observed one.

D. DATA SUMMARY TAPES

From raw data magnetic tapes which were written with the PDP 11/45, we made two kinds of summary tape: edited tapes and data summary tapes (DST). Since the code format of the KEK central computer HITAC 8800 is different from that of the PDP 11/45, raw data written by the PDP 11/45 must be changed in code, making the edited tapes. At this time, various parameters necessary to specify a run in question and trigger condition are associated with the raw data. The data format in these edited tapes are the same as that in the raw data magnetic tapes.

During the course of the data analysis, the track reconstruction and momentum calculation for each event needed long CPU time. To save this time, reconstructed tracks and momentum were written to the data summary tapes, together with various kinematical parameters calculated from these tracks in each event. The event record also contains the trigger conditions, data specifiying the degree of the reconstructions, those from the beam momentum hodoscope etc.

Further analysis of the data to produce the final results was started from DST.

E. IDENTIFICATION OF ELASTIC EVENTS

1. GENERAL

The DST contained measured values of geometrical and kinematical quantities in each event. The first task to be made by using the DST is to determine whether an event is elastic or inelastic. Then the yield distribution of elastic events is obtained as a function of the four momentum transfer of pions.

To distinguish the elastic process from the background ones we used the three constraints for the elastic event as described in Chapter II -A. From the incident beam momentum P_{inc} and the scattering angles Θ_F, ϕ_F of the forward going particle, we calculated expected values for the scattering angles Θ_B, ϕ_B of the backward going particle and the momentum of the forward going particle P_F using the elastic kinematics. The definition of these quantities is given in Fig. 13.

Let the observed scattering angles of the backward going particle be denoted by Θ_B' and ϕ_B' and the observed momentum of the forward going particle using the spectrometer by P_F'. The coplanarity $\Delta\phi$, the angular correlation $\Delta\Theta$ and the momentum correlation ΔP in each event are defined as follows:

$$\Delta\phi = \phi_B - \phi_B',$$

$$\Delta\Theta = \Theta_B - \Theta_B',$$

$$\Delta P = P_F - P_F'.$$

For the elastic event, these three quantities are expected to show a Gaussian distribution with rather narrow width whereas for inelastic events they may have much broader distributions. The standard deviations of the above Gaussian distributions for these three correlations are determined by the resolution of the spectrometer system and are denoted as follows:

$$\sigma_\phi \equiv \sigma_\phi(t) ,$$
$$\sigma_\theta \equiv \sigma_\theta(t) ,$$
$$\sigma_p \equiv \sigma_p(t) ,$$

where t is the four momentum transfer. These may be taken as a resolution function for the corresponding quantities ϕ_B', Θ_B' and P_F'. Now we define the three dimensional phase space of which components are $\Delta\phi$, $\Delta\Theta$ and Δp which are normalized by σ_ϕ, σ_θ and σ_p, respectively. Then the probability of an event being elastic is related to a distance between the origin and a representative point of the event in the phase space.

The value of χ^2 for the event is given by

$$\chi^2 \equiv \left(\frac{\Delta\phi}{\sigma_\phi(t)}\right)^2 + \left(\frac{\Delta\theta}{\sigma_\theta(t)}\right)^2 + \left(\frac{\Delta P}{\sigma_p(t)}\right)^2 .$$

Since $\Delta\phi$, $\Delta\theta$ and Δp have a normal distribution for elastic events, the above χ^2 would have the chi-squared distribution for three degrees of freedom.

When the value of χ^2 for an event as calculated above is smaller than a given value, the event is defined as an elastic one.

2. DETERMINATION OF RESOLUTION FUNCTIONS

To select out the elastic events with the method described in the previous section, we must determine the momentum transfer dependence of the dispersion in the coplanarity, angular correlation and momentum correlation -- resolution functions -- for the elastic events. An exact way to determine this is to make histograms of the coplanarity, angular correlation and momentum correlation at every momentum transfer bin which is the same as used in the final cross section data, and to obtain the momentum transfer dependence in question from the width of Gaussian distribution which corresponds to an aggregation of elastic events in these histograms. This procedure, however, is not applicable to our case because the number of elastic events is often too small to obtain a good enough distribution at a given momentum transfer bin. Accordingly, the following method was adopted:

i) All recorded events in the DST are divided into bins with each 0.05 rad according to their values of Θ_F.

ii) For every bin, the coplanarity, angular correlation and momentum correlations are histogramed, and the dependence of the dispersion for three parameters on Θ_F were determined from the width of the Gaussian peak for the elastic scattering events.

iii) The results thus obtained are fitted by appropriate functions (the resolution functions) from which the dispersions at an arbitary value of the momentum transfer can be calculated.

A typical example of the histograms of the coplanarity, angular correlation and momentum correlation at several scattering angles is shown in Fig. 14. In Figs. 15 ∿ 17, shown are the Θ_F dependences of the dispersions determined by the above procedure.

Qualitative behavior of the θ_F dependences is easily understood when care is taken for the elastic kinematics and the spectrometer resolution including the multiple scattering and energy-loss. The resolution functions used are derived under the approximation that the all elastic events come from a point source. This approximation seems to be enough to study the qualitative behavior of the resolution functions. The coordinate system and the kinematical quantities used in the following discussion are shown in Fig. 13. The resolution functions used are:

i) For the coplanarity,

$$\sigma_\phi^2 = \frac{a_1^2}{\sin^2\theta_F} + \frac{a_2^2}{\sin^2\theta_B} + a_3^2 \frac{E_F^2}{P_F^4 \sin^2\theta_F} + a_4^2 \frac{E_B^2}{P_B^4 \sin^2\theta_B} ,$$

where a_1 and a_2 are the scattering angle resolutions of arm 1 and arm 3, respectively, while a_3 and a_4 are the effective thicknesses of materials through which particles pass in the arm 1 and arm 3 respectively. First two terms come from the spatial resolution of the chambers, while last two are due to the multiple scattering of scattered particles in materials.

ii) For the momentum correlation,

$$\sigma_P^2 = c_1^2 \left[g_1(t) \right]^2 + c_2^2 \left[g_2(t) \right]^2 + c_3^2 P_F^4 + c_4^2 \left[g_1(t) \right]^2 \frac{E_F^2}{P_F^4} ,$$

with

$$g_1(t) = \frac{P_{inc} P_F \sin\theta_F}{P_{inc} \cos\theta_F - \frac{P_F}{E_F} (E_{inc} + m_p)} ,$$

$$g_2(t) = \frac{\frac{P_{inc}}{E_{inc}} (E_F - m_p) - P_F \cos\theta_F}{P_{inc} \cos\theta_F - \frac{P_F}{E_F} (E_{inc} + m_p)} ,$$

$$c_3 = \frac{\Delta\Theta}{0.3 \int B \, dl} ,$$

where c_2 is the momentum acceptance for the incident beam, and numerically we have $c_1 \simeq a_1$ and $c_4 \simeq a_3$. First two terms come from the spatial resolution of the forward arm and the momentum spread of the incident beam, respectively. while the third from the momentum resolution of the spectrometer magnet and the last due to the multiple scattering of the forward going particle.

iii) For the angular correlation,

$$\sigma_\Theta^2 = b_1^2 \, [\, f_1(t) \,]^2 + b_2^2 \, [\, f_2(t) \,]^2 + b_3^2 \frac{E_F^2}{P_F^4} [\, f_1(t) \,]^2 + b_4^2 \frac{E_B^2}{P_B^4} + b_0^2 ,$$

where

$$f_1(t) = \left(\frac{\cos\Theta_F}{P_{inc} - P_F \cos\Theta_F} \right)^2 [\, P_{inc} \, (\, g_1(t) \sin\Theta_F + P_F \cos\Theta_F) - P_F^2 \,] ,$$

$$f_2(t) = \left(\frac{\cos\Theta_F}{P_{inc} - P_F \cos\Theta_F} \right)^2 [\, P_{inc} \, g_2(t) - P_F \,] \sin\Theta_F ,$$

where $b_1 \simeq c_1$, $b_2 \simeq c_2$, $b_3 \simeq a_3$, $b_4 \simeq a_4$ and $b_0 \simeq a_1$. First two terms come from the same origins of the first two terms in σ_p. The third term due to the multiple scattering of the forward scattered particle. The last two terms come from the multiple scattering of the backward scattered particle and the spatial resolution of the chambers in the backward arm, respectively.

The fitted results using these resolution functions are shown in Figs. 15 ∿ 17.

3. SELECTION OF ELASTIC EVENTS

A first step to select the elastic events is to reject events which are not originated from the hydrogen target. An interaction vertex of each event is calculated from the particle trajectories in C1 to C2 and C5 to C6, and events which have the vertex outside the target volume are rejected. The events survived from this selection are served for the χ^2 selection to choose elastic events. In Fig. 18, typical examples of the vertex distribution are shown both for the full and empty targets along the beam axies. In Fig. 19, we give a typical example of the radial distribution in the interaction vertex projected perpenducular to the z-axies.

Next step is the χ^2-selection for elastic events. As discussed in the previous section, the calculated χ^2 for the elastic event is expected to have a χ^2-distribution for three degrees of freedom. The probability of χ^2 having values larger than χ_0^2 for ν degrees of freedom is

$$Q\,(\chi_0^2\ ;\ \nu\,) = \int_{\chi_0^2}^{\infty} \frac{1}{2\Gamma(\frac{\nu}{2})}\left(\frac{\chi^2}{2}\right)^{\frac{\nu}{2}-1} e^{-\frac{\chi^2}{2}}\, d\chi^2 \ .$$

Elastic events are then defined as those in which

$$\chi^2 \leq 11.34\ .$$

The probability of χ^2 being larger than this value is

$$Q\,(\chi^2{=}11.34\ ;\ \nu{=}3\,) = 0.01\ .$$

Typical examples of the χ^2-distribution are shown in Fig.20 at various values of the momentum transfer. As seen in these examples, a clean elastic peak at every momentum transfer implies that the present method has a good validity in selecting elastic events. For inelastic contamination in the above selected events we will give a detailed discussion in the next chapter.

To check the adequacy of the above value of χ^2, the value of χ_0^2 is varied around 11.34 and thus verified that no appreciable change is found, as in Fig.21. The result is also compared with the integral probability $Q(\chi^2;\nu)$ for $\nu=3$ which is shown by the solid line in Fig. 21. As seen in this figure theoretical calculation can well explain the result, which enables us to believe the correctness of our treatment of the data.

IV. CALCULATION OF THE CROSS SECTION

A. GENERAL PROCEDURE

From the yield distribution of the elastic events as a function of t obtained in the previous chapter, we can determine the magnitude of differential cross section. When a care is taken that a certain momentum transfer region is covered by the different types of trigger combinations at the same time, the differential cross section is given by

$$\frac{d\sigma}{dt} = \frac{\eta}{\Delta t \cdot N_T} \sum_i n_i \Big/ \sum_i \frac{A_i}{C_i} B_i ,$$

where η is the correction factor, N_T is the number of target protons, Δt is the width of the momentum transfer bin, n_i is the detected number of the elastic events, A_i is the acceptance, C_i is the count-down factor and B_i is the number of the incident particles for the i-th trigger type.

There are two categories in the correction factors; one is those which are independent on t and the other is those which are dependent on t. The former consists mainly of: (a) the decay and absorption of the incident particles, and (b) the contamination in the incident particles, whereas the latter consists mainly of: (a) the decay and absorption of the scattered particles, (b) the loss in the track reconstruction, (c) the inelastic background contamination, (d) the δ-ray emission, etc.

In the followings, we will discuss a method adopted in the acceptance calculation and a procedure of the corrections listed above.

B. DETERMINATION OF THE DETECTOR ACCEPTANCE

The acceptance of the forward arm of the spectrometer system is defined by T1 and T2. T1 gives a limit in the vertical direction, while T2 does in the horizontal direction of the acceptance. The acceptance of the backward arm is defined by T5 hodoscope both vertically and horizontally. Together with these geometrical conditions of the counters, the finite size of the hydrogen target and the incident beam profile must be taken into account for calculating the acceptance of the spectrometer. The multiple scattering and the energy loss of low energy scattered particle are also taken into account as a non-negligible effect to the acceptance. A Monte-Carlo simulation which takes the above conditions into account has been made to obtain the acceptance as a function of t. Details of this prgram is as follows:

Events are generated uniformly along the incident beam direction in a cylindrical volume, the length and the diameter of which are given by the target length and the beam profile observed by the multiwire proportional chambers. The scattering angle Θ and the azimuthal one ϕ are generated uniformly between 0 and $\pi/4$ rad and 0 and 2π rad, respectively.

The effect of multiple scattering in various materials, namely liquid hydrogen in the target, the vacuum insulator of the target, the plastic scintillators and wire spark chambers, is taken into account according to the following formula for the dispersion of the Gaussian distribution

$$< \Theta > = \frac{15}{p\beta} \sqrt{\frac{L}{L_R}} (1 + \varepsilon) ,$$

where p and β are momentum and velocity of the particle, L is the length of a matter of which radiation length is L_R and ε is the correction factor.

At the same time the energy-loss in these materials is also taken into account according to the following formula:

$$-\frac{dE}{dx} = \frac{0.307}{\beta^2}\frac{Z}{A}\left[\ln\frac{0.511 \times 10^6}{I}\frac{\beta^2}{1-\beta^2} - \beta^2\right] \quad (\mathrm{MeV \cdot cm^2/g}) ,$$

where β is the velocity of the particle, Z and A are the charge and mass number of the material in question, and I is the average ionization potential of the material.

A particle track of the generated event in the magnetic field of the spectrometer is given by solving the equations of motion with a Runge-Kutta method, as discussed in the Chapter III-C. This program to solve the equations of motion is essentially the same one which is used to make the momentum reconstruction.

Among the six trigger types discussed in II-B-6.2, EV1, EV2 and EV3 have been employed when the polarity of the spectrometer magnet is up, while EV4, EV5 and EV6 have been employed when the polarity is down. For each sense of the polarity, a Monte-Carlo simulation has been carried out separately.

In the simulation program, the average time to simulate one event is 30 msec, and total 6×10^5 events have been generated for each polarity. In Fig.22, the acceptance of each event type is shown.

C. DATA CORRECTIONS

1. ATTENUATION OF BEAM

The intensity of the incident beam is attenuated by the decay of pions between B3 counter and the hydrogen target. A correction factor F_d corresponding to this effect is given by

$$F_d = \exp(-d/\eta c\tau),$$

where d is the distance between B3 and the target, $\eta = p/m_\pi$ and $c\tau$ the decay length of pions. This correction amounts to (1.2 ± 0.6)%.

The beam flux is also attenuated by the nuclear absorption in intervening materials such as air and liquid hydrogen. This correction can be estimated by

$$F_a = \exp(-x/\lambda),$$

where x is the path length in liquid hydrogen (only liquid hydrogen contributes appreciably) and λ is the mean free path of pions in liquid hydrogen. With a value λ=790cm at this momentum the average nuclear absorption correction is estimated to be (3.8 ± 0.5)%.

2. BEAM CONTAMINATION

The main contaminations of the incident pion beam are electrons and muons. As described in II-B-5, since a signal from the gas Cherenkov counter is not included in the event trigger logic, the signal BEAM4 contains these contaminations. To give the correction due to these contaminations fractions of electrons and muons are estimated from pressure curve of the gas Cherenkov counter. The result shows that this correction is (3.5 ± 1.5)%.

3. ATTENUATION OF SCATTERED PARTICLES

Scattered particles are lost by the nuclear absorption. The correction factor F'_a due to this effect is given by

$$F'_a(t) = \exp(-\sum_i N_o \rho_i \, x_i(t) \, \sigma_i / A_i),$$

where $N_o \rho_i / A_i$ is the number of nuclei in a unit length of material i, $X_i(t)$ is material thickness traversed by the scattered particle with momentum transfer squared t and σ_i the absorption cross section of the scattered particle for material i. At the present energy the absorption cross section is[27)]

$$\sigma_i \simeq 0.7 \, \sigma_i^{Tot} \quad ,$$

where σ_i^{Tot} is the total cross section of the scattered particle for material i. For protons the total cross section on nuclei is expressed as[28)]

$$\sigma_i^{Tot} = 2\pi R^2 [1 - (1 - (2\kappa + 1) e^{-2\kappa})/2\kappa^2],$$

with $\kappa = R/X_o$, where R is the nuclear radius, and X_o is the absorption length of protons in the nuclear matter. The above equation is also applicable to the pion case if the energy is well above the 33 resonance.[29)]

The correction factor F'_a is calculated at every bin of t; the maximum value is (7.7 ± 1.0)% at $t=-3.8$ $(\mathrm{GeV}/c)^2$ and the minimum is (5.2 ± 1.0)% at -2.8 $(\mathrm{GeV}/c)^2$.

Scattered pions are also lost by the decay. The correction factor F'_d due to the decay is

$$F'_d(t) = R(t) \exp[-d(t)/\eta(t) c\tau],$$

with $\eta(t) = p(t)/m_\pi$, where p(t) is the pion momentum at t in the lab system, and R(t) denotes the probability that the difference in angle or momentum between the parent pion and the daughter muon is greater than the corresponding experimental resolutions. This correction factor is also calculated at every bin of t, amounting to (1.5 ± 1.0)% at $t=-0.25$ $(\mathrm{GeV}/c)^2$ and (4 ± 2)% at -3.75 $(\mathrm{GeV}/c)^2$.

4. δ-RAYS CORRECTION

There is a certain probability that δ-rays produced in the target volume by any of incident and scattered particles in an elastic event hit the veto counters (A1 and A2) and consequently the event is lost. The production probability of the δ-ray of kinetic energy T due to a spinless particle with unit charge of velocity β is

$$d^2N/dTdX = (D/2)\ (1/\beta)^2\ 1/T^2,$$

in an interval between X and X+dX in the target, where $D=0.307\ \mathrm{MeV.cm^2/g}$.

The correction factor F_δ due to this effect is then given by integrating the above equation over the whole target volume,

$$F_\delta = \int_0^L dX \int_{T_{min}}^{T_{max}} dT \frac{d^2N}{dTdX} = \frac{D}{2\beta^2} \int_0^L dX[\ 1/T_{min}(x) - 1/T_{max}(x)],$$

where T_{max} and T_{min} are the maximum kinetic energy of the δ-ray and the minimum one to be able to reach the veto counters, respectively, and L the target length. From the range-energy relation of an electron in hydrogen $T_{min}(X)$ is given by

$$T_{min}(X) = 4.2\ (L - X)^{0.95} + T_o,$$

where T_o is the minimum kinetic energy required for the δ-ray which can escape from the target volume and arrive at the veto counters. A value 2 MeV is assumed for T_o. Integrating the above formula we have $F_\delta = (2 \pm 1)$ %, where the acceptance of the veto counters is taken into account.

5. EMPTY TARGET CORRECTION

This correction is obtained by analyzing the empty-target data in the same way as in the full-target case. Empty-target events which satisfy the same criteria for an elastic event in the full-target case should be due to the elastic scattering on protons other than those in liquid hydrogen. The contribution from these empty-target events must be subtracted and this correction amounts to 2% at small angles while 4% at large angles.

6. INELASTIC BACKGROUND CORRECTION

An unwanted admixture of inelastic events is determined in the following manner. First we assume that in the event fitting inelastic events have the χ^2-distribution different from that for elastic ones; in fact it seems to be reasonable that the latter show a typical peaked structure, while the former is distributed rather widely. So that the χ^2 distribution at larger values of χ^2, which is assumed to be purely due to inelastic events, is extrapolated into the smaller χ^2 values. This extrapolated result gives the correction factor in question; it amounts to 6% at small values of $|t|$, while 2% at larger $|t|$.

7. TRACKING INEFFICIENCY

In making the elastic event selection, we have imposed a condition that at least one trajectory must be found in each of three groups of chambers, namely, C1 and C2, C3 and C4, and C5 and C6, as has already discussed in III-E. Events which do not satisfy this condition are omitted from further analysis. The degree of event loss due to this selection is dependent upon the efficiency of the chambers. The overall tracking efficiency is obtained by averaging the product of tracking efficiencies for three groups of chambers over all runs. The results are that the correction due to the tracking inefficiency is 12% for trigger modes EV1, EV2 and EV3, while it is 19.8% for EV4 and EV5.

Events are also lost when an inadequate combination of the three trajectories is chosen. This loss can be estimated from a probability that the momentum reconstruction program can not find a solution for the particle momentum using the given combination of the trajectries before and after the spectrometer magnet. This correction is found to be independent of the trigger type and estimated to be 11%.

8. SUMMARY OF SYSTEMATIC ERRORS

In Table 5 systematic errors in the present experiment are summarized. The total systematic error is estimated to be 11%.

V. RESULTS AND DISCUSSIONS

A. RESULTS

Results of the differential cross section (DCS) as a function of t are shown in Fig. 23. Numerical values of the DCS are tabulated as a function of t as well as of the CM angle in Table 6. The errors quoted are only of statistical origin. A lack of the data in the vicinity of $-t=1.6$ $(GeV/c)^2$ is due to the fact that the acceptance of the spectrometer system can not extend to this region.

The most salient features of the results are as follows:

i) Prominent forward and backward peaks.
ii) A first dip near $-t=0.7$ $(GeV/c)^2$.
iii) A secondary broad peak.
iv) A sharp dip at $-t=2.5$ $(GeV/c)^2$.
v) A sharp dip at $-t=3.2$ $(GeV/c)^2$.

There are three other experiments which have measured all angles at around the same momenta.[30),31),32)] In the forward region, the results of these three experiments are consistent with the present ones. At larger angles, though the statistics is very poor, ref. 32) shows a dip around $-t=2.8$ $(GeV/c)^2$ and other two data are more or less similar to this again with poor statistics whereas the present data reveal two clear dips at $-t=2.5$ and 3.2 $(GeV/c)^2$. There are two other experiments at around the same momenta but have measured over a limited range of scattering angles.[33),34)] The experiment of ref.33) in a range of $2.37<-t<2.9$ $(GeV/c)^2$ shows a dip at $-t=2.6$ $(GeV/c)^2$, which coincides with the present second dip, while the experiment of ref.34) in a range $-0.8<u<0.06$ $(GeV/c)^2$ gives a dip at around $-t=3.3$ $(GeV/c)^2$, which is also the same as the present third one.

From these observations it should be emphasized that the present data show a good agreement with others only in cases when these other data have enough statistics. In addition to this, the present data clarify not only the position of dips but also the magnitude of DCS even at the bottom of the dips to a remarkable statistical accuracy only by a single measurement. In Fig. 24, the data of older experiments are compiled and compared with the present ones.

B. COMPARISON WITH PHASE SHIFT ANALYSES

There are two sets of phase shift analysis so far performed up to the present energy region; the Saclay analysis[3)] and the Karlsruhe-Helsinki one.[4)] The former uses the shortest path method which allows to give the most continuous solution as a function of energy. The maximum value of orbital angular momentum ℓ_{max} included in the analysis is 5. The latter uses the fixed-t dispersion relation to make a solution obtained as smooth as possible with respect to energy. Starting from the forward amplitudes which are given by the forward dispersion relation the analysis is extended to higher $|t|$ values step by step at intervals of small $|t|$. With this method, a set of solutions has been obtained up to 6 GeV/c.

In Fig. 25, results of these two sets are compared with the present data. In the forward peak region both solutions give a good fit. In the secondary peak region, the Karlsruhe-Helsinki solution still shows a good fit, whereas the Saclay one at 2.548 GeV/c gives too small values. At larger $|t|$, the present data exhibit clear two dips, while neither of these solutions can reproduce this behavior. In the backward peak region, again neither of them can fit the data.

From these observations it can be concluded that the existing sets of phase shift analysis are by no means sufficient one. It is therefore necessary to make a new phase shift analysis in which the present data, particularly those at larger $|t|$, will play an important role.

C. LEGENDRE FIT

In order to obtain a rough idea of the implication of the present data, we make a simple fit to the data using the Legendre polynomials. The DCS is expanded as follows:

$$\frac{d\sigma}{dt} = \sum_{\ell=0}^{\ell_{max}} a_\ell P_\ell(\cos\theta).$$

First, we determine the value of ℓ_{max} in a way that when an increase of ℓ_{max} causes no appreciable change in χ^2 per degree of freedom. In Fig. 26, χ^2/D.F. is shown as a function of ℓ_{max}. From this figure it is clear that $\ell_{max}=17$ is enough to reproduce the data. The result of this fit with $\ell_{max}=17$ is shown in Fig. 25. Furthermore Fig. 27 shows relative coefficients normalized to a_0 as a function of ℓ, together with those given by the phase shift analysis of the Karlsruhe-Helsinki group for comparison.

Fig. 27 implies that the value of ℓ at which a_ℓ reaches its maximum is almost the same ($4\sim5$) both in these two results, whereas at values larger than $\ell=6$ the Karlsruhe-Helsinki result shows much smaller coefficients. This difference may be due to the fact that in the Karlsruhe-Helsinki analysis ℓ_{max} is taken to be 12, while in the present case $\ell_{max}=17$. This means that in a future analysis one must take into account the effect of partial waves higher than at least $\ell=6$.

Another conclusion obtainable from the present analysis is that the behavior of a_ℓ as a function of ℓ obviously suggests a peripheral nature of the $\pi^- p$ interactions at this energy.

D. SEARCH FOR ERICSON FLUCTUATIONS

In the π^+p elastic scattering at 5 GeV/c, Schmidt et al.[18)] have found a rapid variation in the angular distribution with energy at large angles. They have claimed that this rapid variation is nothing but the so-called Ericson fluctuations.[19)] In fact they have obtained two sets of the DCS data in two adjacent energy intervals whose central values are spaced only by 36 MeV in the CMS energy, and calculated an asymmetry parameter A(t) which is defined as follows:

$$A(t) = \frac{\sigma(t,\ \text{high}) - \sigma(t,\ \text{low})}{\sigma(t,\ \text{high}) + \sigma(t,\ \text{low})},$$

where $\sigma(t,\ \text{high})$ and $\sigma(t,\ \text{low})$ are the DCS at t in the higher and lower energy intervals, respectively.

The results show that in the π^+p a clear oscillating behavior of A(t) is observed above $|t| = 2\ (\text{GeV/c})^2$, while in the π^-p no such an indication is found. This conclusion, however, does not seem to be unambiguously confirmed and therefore it is of much interest to examine whether the Ericson fluctuations are observed or not even at the present energy. To this end we divided the data in the following way. The beam momentum is defined by the beam hodoscope consisting of eight overlapping pieces of scintillation counter as has already described in II-B-1. Making appropriate combination of the hodoscope signals we have totally 20 bins. A momentum dispersion at the hodoscope is bin width per $\Delta p/p=0.25\%$. We first divided the data into two groups (Set H_1 and L_1) which corresponded to the upper and lower half of the hodoscope bins, respectively, a spacing between average values of the CMS energy for these groups being 10 MeV. However, owing to a finite resolution of the counter, exact values of the momentum for these groups are partially overlapped. To get a better separation in momentum we excluded a part of the data which corresponded to a central part of the hodoscope bins. Thus we have other three sets of the data grouping (Sets 2 to 4), according to the degree of the separation; Set H_4 and L_4 has the highest separation in momentum at the cost of the decrease in statistics.

Now the asymmetry A_i (t) for each Set i is given by

$$A_i(t) = \frac{N(H_i) - N(L_i)}{N(H_i) + N(L_i)} ,$$

where $N(H_i)$ and $N(L_i)$ are the number of events in the i-th Set H and L, respectively. Results are shown in Fig. 28, where the event distribution in the hodoscope bins is also displayed. From this figure one can easily see that neither of these four sets show any clear indication of the Ericson fluctuations.

VI. CONCLUSIONS

The differential cross section for the $\pi^- p$ elastic scattering has been successfully measured with a high statistics at an incident momentum of 2.46 GeV/c. The present experiment covers a wide range of momentum transfer squared $0.05 \lesssim |t| \lesssim 3.7$ $(\mathrm{GeV/c})^2$ using a single setup which consists of a large aperture spectrometer placed in the forward direction and the other track detector system at a large angle. The present results show two pronounced dips at $|t|=2.5$ and 3.2 $(\mathrm{GeV/c})^2$ besides the well-known dip at $|t|=0.7$ $(\mathrm{GeV/c})^2$. A few experiments so far performed have shown some indication of these dips, but only in a qualitative way in some case or separately in other cases. On the other hand, the present measurement clarifies the whole behavior of the DCS at these large angles at the same time with a high statistical accuracy.

Implications resulting from the comparison of the data with the two sets of phase shift analysis, the Saclay and the Karlsruhe-Helsinki ones, are as follows: In the secondary peak region, the latter gives a good fit to the present data, whereas the former gives too small values. At larger values of $|t|$ above the second dip, neither of them reproduces any detailed structure of the data. Thus it should be necessary to make a new phase shift analysis by taking into account the present data.

The data are also fitted by a series of Legendre polynomials. It is found that the highest order of the polynomials required to reproduce the data very well is at least 15 or 16. Polynomials of order 4 and 5 make the largest contribution and the higher ones give contributions gradually decreasing with the order of polynomials. This behavior indicates a typical peripheral nature of the $\pi^- p$ interactions at this energy.

Finally a possible evidence for Ericson fluctuations is examined by dividing the data into two groups according to a small difference between their incident momenta, the spacing between them being 10.0 MeV in the CMS energy. The asymmetry parameter is calculated by using these two groups of the data, but the result is negative; we have found no evidence for Ericson fluctuations. We can thus conclude that some of conditions which are required to realize Ericson fluctuations are not yet satisfied at this energy, or the physical picture which is depicted by the statistical bootstrap theory has something bad in describing the π^-p interactions.

REFERENCES

1) For the summary of the experiments on the pion-nucleon elastic scattering, see R.L. Kelly, Review talk in "New Directions in Hadron Spectroscopy", ANL-HEP-CP-75-58.

2) S. Almehed and C. Lovelace, Nucl. Phys. B40, 157(1972).

3) R. Ayed and P. Bareyre, as quoted by the Particle Data Group, Rev. Mod. Phys. 48, S1(1976).

4) E. Pietarinen, Paper submitted to the Topical Conference on Baryon Resonances, Oxford, July 1976.

5) R.E. Cutkosky, R.E. Hendrick, Y.A. Chao, R.G. Lipes, J.C. Sandusky, R.L. Kelly and J.W. Alcock, Paper submitted to the Topical Conference on Baryon Resonances, Oxford, July 1976.

6) R.P. Feynman, M. Kislinger and F. Ravndal, Phys. Rev. D3, 2706(1971).

7) S. Mandelstam, Phys. Rep. 13C, 260(1974).

8) Chodos, R.L. Jaffe, K. Johnson, C.B. Thorn and V.F. Weisskoff, Phys. Rev. D9, 3471(1974); W.A. Bardeen. M.S. Chanowitz, S.D. Drell, M. Weinstein and T.M. Yan, Phys. Rev. D11, 1094(1975).

9) J. Schwarz, Phys. Rep. 8C, 269(1973).

10) E. Ma and G.L. Shaw, Phys. Rev. D13, 3027(1976).

11) A.W. Hendry, Phys. Rev. Letters 41, 222(1978).

12) G. Höhler, H.P. Jakos, F. Kaiser and G. Brandenburger, TKP 78-10.

13) See for example, P.D.B. Collins, Phys. Rep. 1C, 103(1971).

14) V. Berger and R.J.N. Phillips, Phys. Rev. 187, 2210(1969).

15) H. Harari, Phys. Rev. Letters 20, 1395(1968); P.G.O. Freund, Phys. Rev. Letters 20, 235(1968).

16) Y. Hara, T. Kuroda and Y. Takaiwa, Prog. Theor. Phys. 51, 840(1974).

17) Y. Hara and T. Kuroda, Prog. Theor. Phys. 53, 1058(1976); T. Kuroda, Prog. Theor. Phys. 57, 2013(1977).

18) F.H. Schmidt, C. Baglin, P.J. Carlson, A. Eide, V. Gracco, E. Johansson and A. Lundby, Phys. Letters 45B, 157(1973).

19) P.J. Carlson, Phys. Letters 45B, 161(1973), see also S. Frautschi, Nuovo Cim. 12A, 133(1972) ; C.J. Hamer, Nucl. Phys. B105, 153(1976).

20) G. Charpak, H.G. Fisher, C.R. Gruhn, A. Minten, F. Sauli, G. Plch and G. Flügge, Nucl. Instr. Meth. 99, 279(1972).

21) K. Amako, S. Inaba, Y. Inagaki and T. Tsuru, KEK-EXP. FACILITIES-3 (in Japanese), July 1976.

22) K. Amako, K. Kawano, T. Matsui and S. Sugimoto, KEK-78-15, October 1978 and KEK-EXP. FACILITIES-78-8, October 1978.

23) T. Tauchi, Master Thesis, Nagoya University, March 1978 (in Japanese, unpublished).

24) T. Tsuru, K. Amako, S. Inaba and Y. Inagaki, KEK-EXP. FACILITIES-5 (in Japanese), July 1976.

25) T. Shimomura, to be submitted as a Ph. D. Thesis, Nagoya University, 1979.

26) B. Zacharov, Nucl. Instr. Meth. 33, 136(1965).

27) R.E. Pollock and G. Schrank, Phys. Rev. 140B, 575(1965).

28) Landolt-Börnstein, New Series I, vol. 7.

29) J. Hüfner, Phys. Rep. 21C, 1(1975).

30) W. Busza, B.G. Duff, D.A. Garbutt, F.F. Heymann, C.C. Nimmon, K.M. Potter, T.P. Swtman, E.H. Bellamy, T.F. Buckley, R.W. Dobinson, P.V. March, J.A. Strong and R.N.F. Walker, Phys. Rev. 180, 1339(1969).

31) P.S. Aplin, I.M. Cowan, W.M. Gibson, R.S. Gilmore, K. Green, J. Malos, V.J. Smith, D.L. Ward, M.A.R. Kemp, A.T. Lea, R. McKenzie and G.C. Oades, Nucl. Phys. B32, 253(1971).

32) C.T. Coffin, N. Dikmen, L. Ettlinger, D. Meyer, A. Saulys, K. Terwilliger and D. Williams, Phys. Rev. 159, 1169(1967).

33) M. Fellinger, E. Gutman, R.C. Lamb, F.C. Peterson, L.S. Schroeder, R.C. Chase, E. Coleman and T.G. Rhoades, Phys. Rev. Letters 23, 600(1969).

34) R.R. Crittenden, K.F. Galloway, R.M. Heinz, H.A. Neal and R.A. Sidwell, Phys. Rev. D1, 3050(1970).

TABLE CAPTIONS

Table 1. Summary of the dimension of multiwire proportional chambers used in the present experiment.

Table 2. Summary of the dimension of scintillation counters used in the present experiment.

Table 3. Summary of the dimension of wire spark chambers used in the present experiment.

Table 4. Position dependence of the efficiency of the wire spark chamber, where m is the value of high voltage at which the efficiency in a given area reaches 50%, $\langle m \rangle$ is the average value of m over the whole effective area of the chamber and s is the difference between values of high voltage required to get the efficiency of 10% and 90%.

Table 5. Summary of the systematic errors in the present experiment.

Table 6. Results of the differential cross section measured in the present experiment at 2.46 GeV/c. Errors are of statistical origin.

Chamber name	Wire direction	Z-position (mm)	Effective area (mm^2)
BPC 1-1	x	-2315	128 × 128
BPC 1-2	y	-2303	128 × 128
BPC 2-1	x	-1578	128 × 128
BPC 2-2	y	-1566	128 × 128
BPC 3-1	x	- 942	128 × 128
BPC 3-2	y	- 930	128 × 128

Table 1

Counter name	Horizontal (mm)	Vertical (mm)	Thickness (mm)	Z-position (mm)
T1 - 0	156	280	5	1419
T1 - 1 ∿ 2	1000	118	5	1419
T2 - 1 ∿ 3	100	300	3	1555
T2 - 4 ∿ 8	200	300	3	1555
T3 - 1 ∿ 13	240	742	10	4430
T4	1010	140	5	276
T5 - 1 ∿ 12	490	400	10	1640
LC - 1 ∿ 6	320	800	50	1784

Table 2

Chamber name	Chamber type	Wire angle with vertical axies	Z-position (mm)	Effective area (mm^2)
C1 - 1	X	0.0°	744.5	1000 × 300
2	Y	90.0°	777.1	1000 × 300
3	V	-15.8°	825.5	1000 × 300
4	U	15.0°	858.3	1000 × 300
5	Y	90.0°	903.0	1000 × 300
6	X	0.0°	936.5	1000 × 300
C2 - 1	X	0.0°	1084.5	1500 × 400
2	Y	30.0°	1117.8	1500 × 400
3	U	14.5°	1163.0	1500 × 400
4	V	-15.0°	1196.4	1500 × 400
5	Y	90.0°	1241.5	1500 × 400
6	X	0.0°	1274.3	1500 × 400
C3 - 1A	X	0.0°	3290.5	2500 × 800
1B	U	30.0°	3290.5	2500 × 800
2A	X	0.0°	3393.5	2500 × 800
2B	V	-30.0°	3393.5	2500 × 800
3A	X	0.0°	3504.5	2500 × 800
3B	U	30.0°	3504.5	2500 × 800
C4 - 1A	X	0.0°	4049.7	3000 × 800
1B	U	30.0°	4049.7	3000 × 800
2A	X	0.0°	4184.3	3000 × 800
2B	V	-30.0°	4184.3	3000 × 800
3A	X	0.0°	4311.9	3000 × 800
3B	U	30.0°	4311.9	3000 × 800
C5 - 1A	U	25.1°	745.3	2000 × 500
1B	X	0.0°	745.3	2000 × 500
2A	V	-24.9°	845.8	2000 × 500
2B	X	0.0°	845.8	2000 × 500
3A	V	-24.6°	945.0	2000 × 500
3B	X	0.0°	945.0	2000 × 500
C6 - 1A	X	0.0°	1253.0	3000 × 800
1B	U	30.0°	1253.0	3000 × 800
2A	X	0.0°	1378.0	3000 × 800
2B	V	-30.0°	1378.0	3000 × 800
3A	X	0.0°	1495.0	3000 × 800
3B	U	30.0°	1495.0	3000 × 800

Table 3

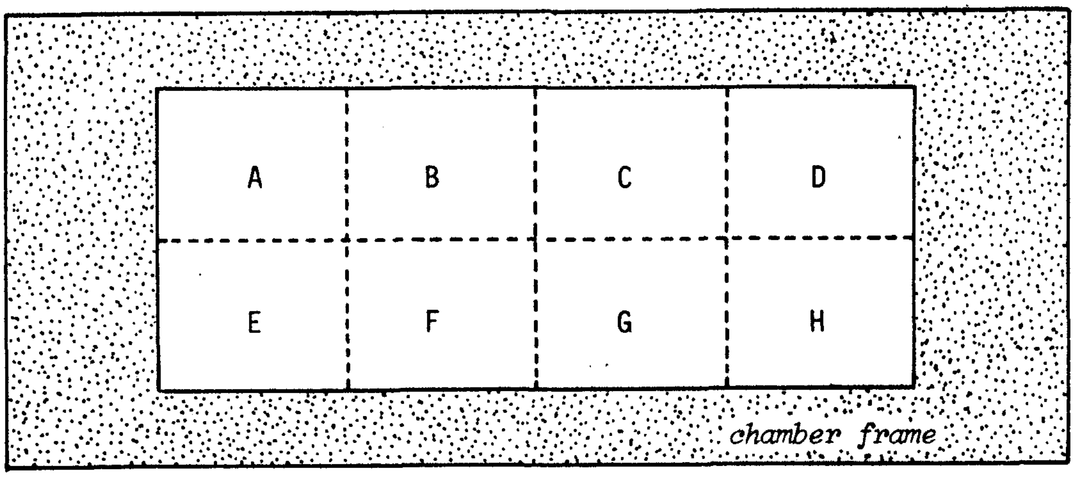

measured position of the local efficiency

position	m (kV)	$\frac{m - \langle m \rangle}{m}$ (%)	s (kV)
A	8.55	7.8	0.30
B	7.60	-3.7	0.55
C	7.70	-4.3	0.60
D	7.85	-0.3	0.45
E	8.35	5.6	0.50
F	7.70	-2.3	0.60
G	7.60	-3.7	0.45
H	7.70	-4.3	0.50

Table 4

Decay correction of beam	0.6 %
Absorption correction of beam	0.5 %
Beam contamination correction	1.5 %
Decay correction of scattered particles	2 %
Absorption correction of scattered particles	2 %
δ-ray correction	1 %
Empty target correction	2 %
Inelastic background correction	2 %
Tracking inefficiency correction	< 10 %
Total	< 11 %

Table 5

-t	dσ/dt	Error	cos θ_{cm}	dσ/dΩ	Error
	mb/(GeV/c)^2			mb/sr	
0.12	17.0	0.44	0.937	5.22	0.15
0.17	9.38	0.33	0.912	2.88	0.10
0.22	6.62	0.28	0.887	2.03	0.086
0.27	7.03	0.29	0.862	2.16	0.089
0.32	5.13	0.25	0.837	1.58	0.077
0.36	3.44	0.21	0.812	1.06	0.065
0.41	2.39	0.18	0.786	0.734	0.055
0.46	1.98	0.083	0.761	0.608	0.026
0.51	1.13	0.045	0.736	0.347	0.014
0.56	0.578	0.025	0.711	0.177	0.0077
0.61	0.408	0.019	0.686	0.125	0.0058
0.66	0.378	0.018	0.660	0.116	0.0055
0.70	0.290	0.015	0.635	0.0890	0.0045
0.75	0.268	0.013	0.610	0.0823	0.0039
0.80	0.295	0.013	0.585	0.0906	0.0040
0.85	0.305	0.013	0.560	0.0936	0.0040
0.90	0.356	0.015	0.534	0.109	0.0046
0.95	0.318	0.014	0.509	0.0976	0.0043
1.00	0.387	0.016	0.484	0.119	0.0049
1.05	0.407	0.016	0.458	0.125	0.0049
1.09	0.456	0.018	0.433	0.140	0.0055
1.14	0.461	0.018	0.408	0.142	0.0055
1.19	0.446	0.018	0.383	0.137	0.0055
1.24	0.538	0.020	0.357	0.165	0.0061
1.29	0.512	0.021	0.332	0.157	0.0065
1.34	0.558	0.023	0.307	0.171	0.0071
1.39	0.599	0.027	0.281	0.184	0.0083
1.73	0.660	0.039	0.104	0.203	0.012
1.78	0.657	0.035	0.078	0.202	0.011
1.83	0.487	0.026	0.053	0.149	0.0080
1.88	0.358	0.021	0.027	0.110	0.0065
1.93	0.346	0.018	0.002	0.106	0.0055

Table 6

-t	dσ/dt mb/(GeV/c)^2	Error mb/(GeV/c)^2	cos θ_{cm}	dσ/dΩ mb/sr	Error mb/sr
1.97	0.306	0.016	-0.024	0.0939	0.0049
2.02	0.263	0.014	-0.049	0.0807	0.0043
2.07	0.195	0.012	-0.074	0.0599	0.0037
2.12	0.159	0.011	-0.100	0.0488	0.0034
2.17	0.129	0.0094	-0.125	0.0396	0.0029
2.22	0.0944	0.0079	-0.151	0.0290	0.0024
2.27	0.0545	0.0058	-0.176	0.0167	0.0018
2.32	0.0404	0.0054	-0.202	0.0124	0.0017
2.37	0.0324	0.0048	-0.227	0.00995	0.0015
2.42	0.0227	0.0037	-0.253	0.00697	0.0011
2.49	0.0144	0.0021	-0.291	0.00442	0.00065
2.59	0.0177	0.0023	-0.342	0.00543	0.00071
2.69	0.0231	0.0026	-0.393	0.00709	0.00080
2.79	0.0284	0.0030	-0.445	0.00872	0.00092
2.89	0.0343	0.0028	-0.496	0.0105	0.00086
2.96	0.0307	0.0035	-0.534	0.00942	0.0011
3.01	0.0295	0.0034	-0.560	0.00906	0.0010
3.06	0.0254	0.0030	-0.585	0.00780	0.00092
3.11	0.0221	0.0027	-0.611	0.00678	0.00083
3.16	0.0155	0.0022	-0.637	0.00476	0.00068
3.21	0.0129	0.0019	-0.662	0.00396	0.00058
3.26	0.0158	0.0022	-0.688	0.00485	0.00068
3.31	0.0259	0.0029	-0.714	0.00795	0.00089
3.36	0.0364	0.0034	-0.739	0.0112	0.0010
3.41	0.0403	0.0038	-0.765	0.0124	0.0012
3.46	0.0496	0.0039	-0.791	0.0152	0.0012
3.50	0.0433	0.0035	-0.817	0.0133	0.0011
3.55	0.0543	0.0039	-0.842	0.0167	0.0012
3.60	0.0864	0.0052	-0.868	0.0265	0.0016
3.65	0.153	0.0092	-0.894	0.0470	0.0028
3.70	0.107	0.015	-0.920	0.0328	0.0046

Table 6 (continued)

FIGURE CAPTIONS

Fig. 1. Layout of the present experimental apparatus.

Fig. 2a. Layout of the beam lines in the experimental hall at KEK.

Fig. 2b. Top view of the beam line $\pi 2$.

Fig. 3. Exploded view of a multiwire proportional chamber.

Fig. 4. Typical example of the high voltage curve for the multiwire proportional chamber. Open circles are the data obtained by using a radioactive source ^{90}Sr, while closed ones are those by the pion beam.

Fig. 5. Details of the hydrogen target and veto counters A1 and A2.

Fig. 6. Bird eye's view of the whole system of counters.

Fig. 7. Exploded view of a wire spark chamber.

Fig. 8. Typical examples of the high voltage curve for the wire spark chamber; closed circles are the efficiency for a single track, open circles for a double tracks and closed triangles for a tripple track.

Fig. 9. Typical examples of the delay curve for the wire spark chamber. Dependence on the clearing field is also studied; closed circles are the data for the clearing field of 100 V, open circles for 70 V and closed triangles for 50 V.

Fig. 10. Schematic diagram of the data aquisition system.

Fig. 11. Data format of an event in the raw data magnetic tape.

Fig. 12. Typical example of particle tracks displayed on the Sony-Tektronix 4010.

Fig. 13. Definition of the coordinate system discussed in Chapter III-E.

Fig. 14. Typical examples of the distributions of coplanarity ($\Delta\phi$), angular correlation ($\Delta\Theta$) and momentum correlation (Δp) at three angular intervals of which central values are lab. angles of 0.2, 0.4 and 0.6 rad, respectively, with the width of the intervals being 0.05 rad.

Fig. 15. Coplanarity distributions as a function of scattering angle for pion forward and proton forward events separately. Solid curves are calculated results from the resolution function given in III-E-2.

Fig. 16. Similar results for the angular correlation as in Fig. 15.

Fig. 17. Similar results for momentum correlation as in Fig. 15.

Fig. 18a. Vertex distribution along the beam axis for the full target.

Fig. 18b. Similar result for the empty target as in Fig. 18a.

Fig. 19. Radial distribution of the interaction vertex projected perpendicular to the beam axis.

Fig. 20. Typical examples of χ^2-distribution at three intervals of t with a width of 0.05 $(\text{GeV}/c)^2$, centered at $-t=0.7$, 1.25 and 3.7 $(\text{GeV}/c)^2$.

Fig. 21. Number of elastic event as a function of χ^2 at $-t=1.0$, 2.0 and 3.0 $(\text{GeV}/c)^2$. Event number at each t is normalized to that at $\chi_0^2=11.34$. Solid curve is the result calculated with the probability distribution function for χ^2 for the degree of freedom of 3.

Fig. 22. Acceptance as a function of t for the magnet polarity up and down. The number of a small circle denotes the trigger type.

Fig. 23. Differential cross section for the π^-p elastic scattering at 2.46 GeV/c as a function of t. Errors quoted are only of statistical origin.

Fig. 24. Similar results obtained by other experiments as in Fig. 23; o Coffin et al. (1967) 2.49 GeV/c, Δ Fellinger et al. (1969) 2.51 GeV/c, ∇ Crittenden et al. (1970) 2.50 GeV/c and □ Aplin et al. (1971) 2.49 GeV/c. Solid curve is drawn by eye by connecting the present experimental data smoothly.

Fig. 25. Comparson of the present data with the results of the phase shift analysis; dashed curve is calculated from Saclay phase shifts, while dash-and-dotted one from Karlsruhe-Helsinki phase shifts. Solid curve is the result of the Legendre fit up to the order of 17.

Fig. 26. χ^2 per degree of freedom as a function of maximum order of the Legendre polynomial taken in the Legendre fit.

Fig. 27. Relative coefficients of Legendre polynomials as a function of the order of polynomial, normalized to the zeroth coefficient a_o; o for odd ℓ and ● for even ℓ. Those calculated from the Karlsruhe-Helsinki phase shifts are denoted by Δ.

Fig. 28. Test of Ericson fluctuations; left: event distribution for four sets of grouping, right: the asymmetry parameter A plotted as a function of t. Errors are only of statistical origin.

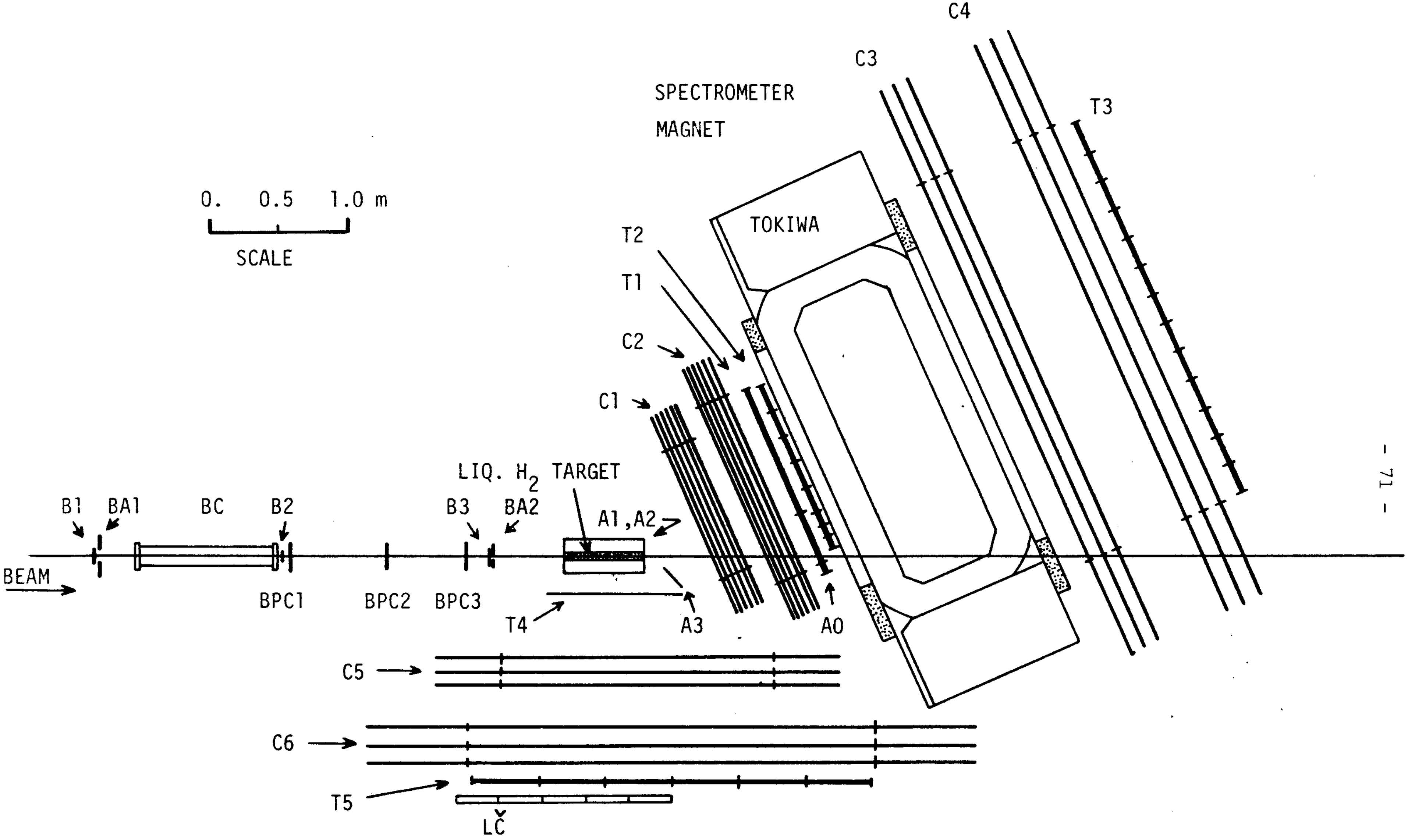
C4
C3
SPECTROMETER
MAGNET
T3
0. 0.5 1.0 m
SCALE
TOKIWA
T2
T1
C2
C1
LIQ. H2 TARGET
B1
BA1
BC
B2
B3
BA2
A1,A2
BEAM
BPC1
BPC2
BPC3
T4
A3
A0
C5
C6
T5
LČ

Fig. 1

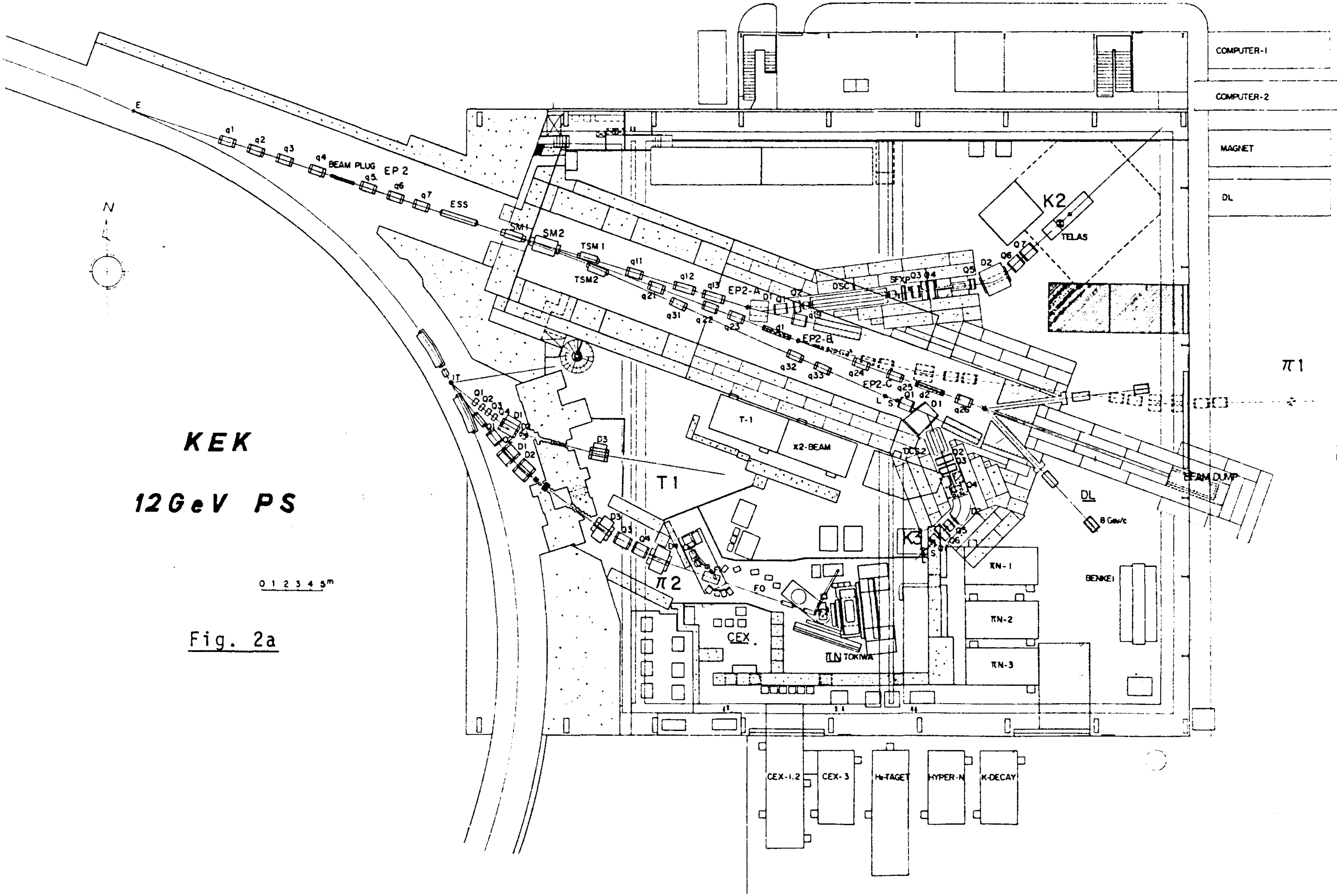
KEK
12GeV PS
N
0 1 2 3 4 5 m
E
q1
q2
q3
q4
BEAM PLUG
EP2
q5
q6
q7
ESS
SM1
SM2
TSM1
TSM2
q11
q12
q13
q21
q22
q23
q31
EP2-A
D1
Q1
Q2
q19
d1
EP2-B
q32
q33
q24
q25
EP2-C
L
S
Q1
d2
D1
q26
OSC
SFXP
Q3
Q4
Q5
D2
Q6
Q7
K2
TELAS
π1
BEAM DUMP
DL
8 Gev/c
T-1
π2-BEAM
T1
DCS2
D2
Q3
Q4
Q2
Q5
Q6
K3
S
πN-1
πN-2
πN-3
BENKEI
IT
Q1
Q2
Q3
Q4
D1
D2
D3
Q3
Q4
D
F1
F0
π2
CEX
πN TOKIWA
COMPUTER-1
COMPUTER-2
MAGNET
DL
CEX-1.2
CEX-3
H-TAGET
HYPER-N
K-DECAY

Fig. 2a

Fig. 2b

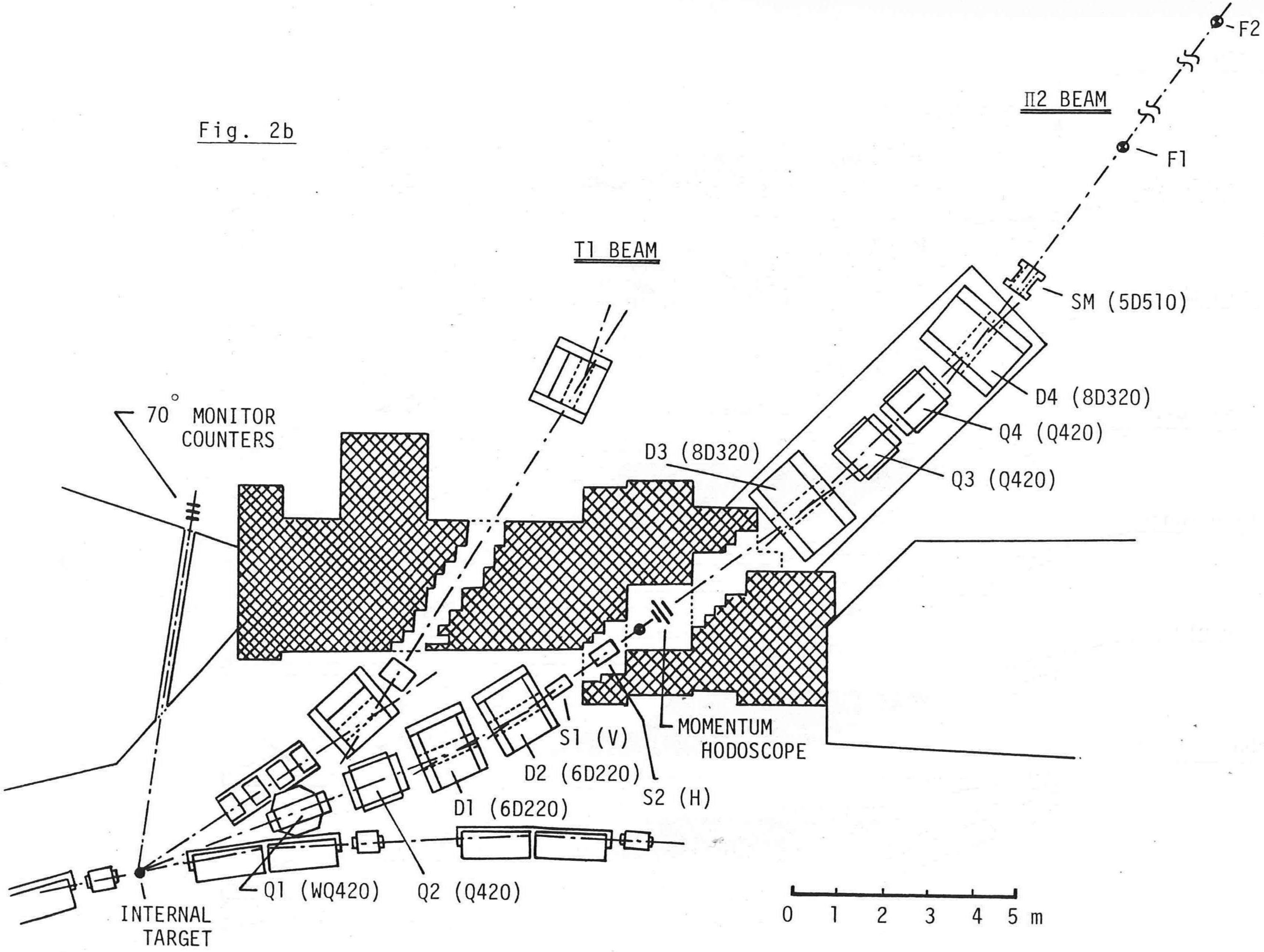
F2
Π2 BEAM
F1
T1 BEAM
SM (5D510)
D4 (8D320)
70° MONITOR COUNTERS
Q4 (Q420)
D3 (8D320)
Q3 (Q420)
MOMENTUM HODOSCOPE
S1 (V)
D2 (6D220)
S2 (H)
D1 (6D220)
Q1 (WQ420)
Q2 (Q420)
INTERNAL TARGET
0
1
2
3
4
5 m

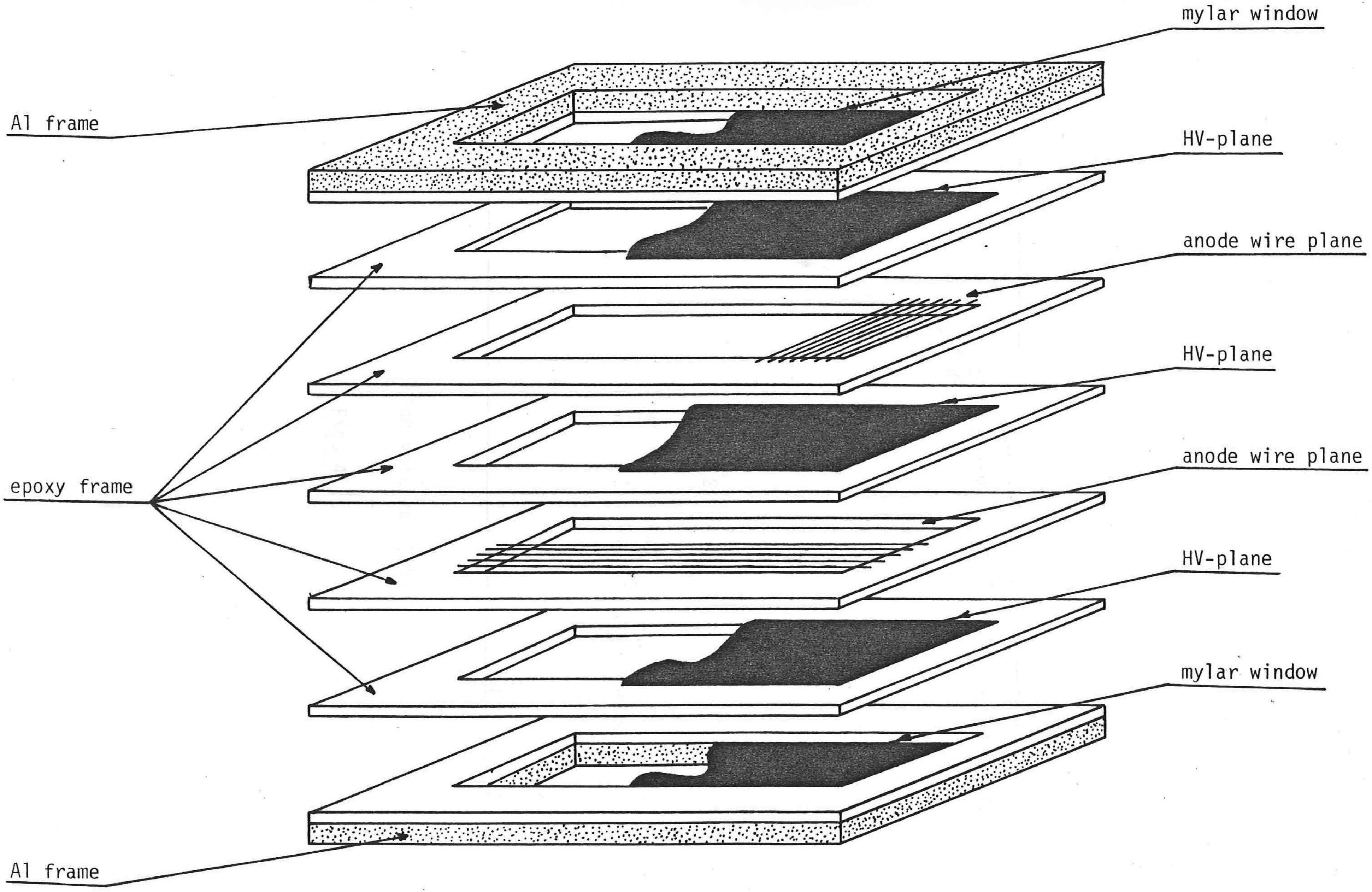
mylar window
Al frame
HV-plane
anode wire plane
HV-plane
anode wire plane
epoxy frame
HV-plane
mylar window
Al frame

Fig. 3

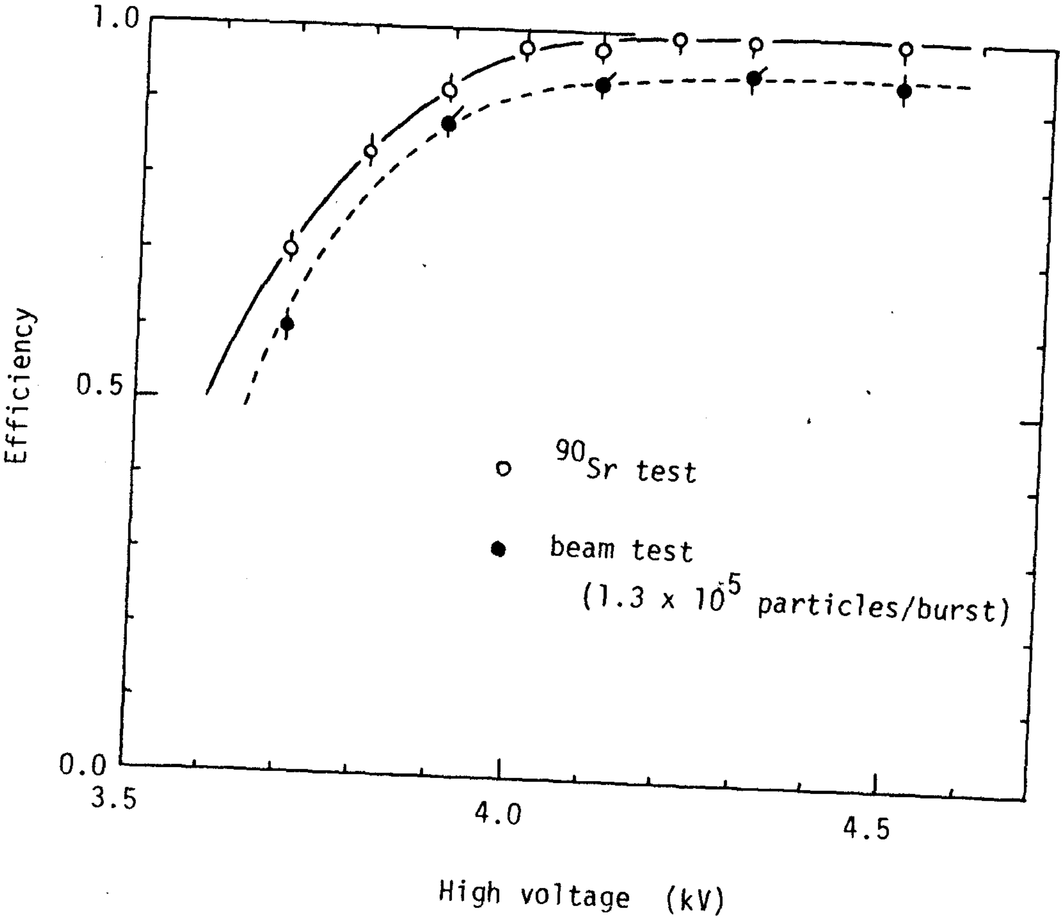
1.0
0.5
0.0
3.5
4.0
4.5
Efficiency
High voltage (kV)
○ ^{90}Sr test
● beam test
(1.3 x 10^{5} particles/burst)

Fig. 4

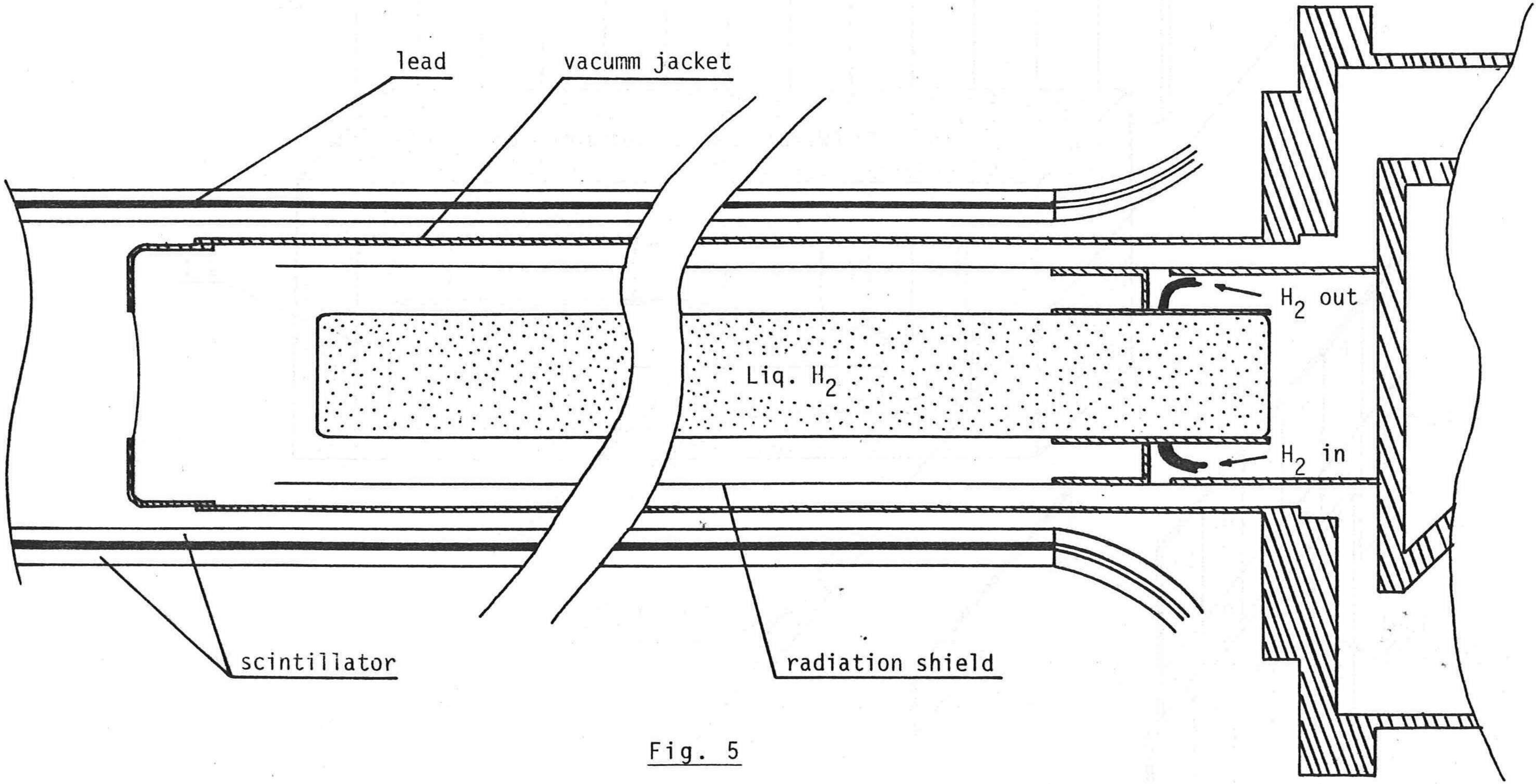
lead
vacumm jacket
H_2 out
Liq. H_2
H_2 in
scintillator
radiation shield

Fig. 5

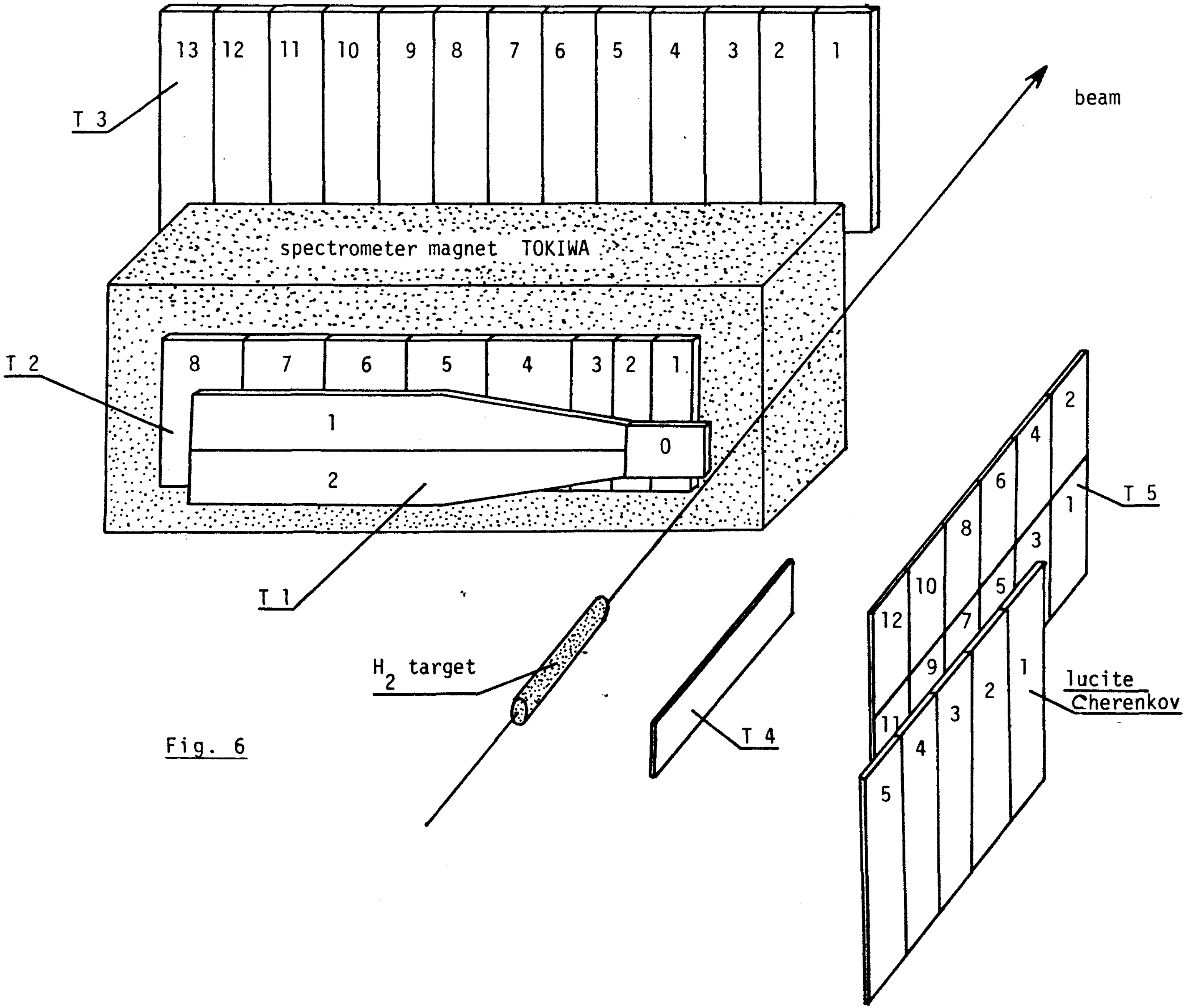
T 3
13
12
11
10
9
8
7
6
5
4
3
2
1
beam
spectrometer magnet TOKIWA
T 2
8
7
6
5
4
3
2
1
1
2
0
T 1
H_2 target
T 4
T 5
2
4
1
6
3
8
5
10
7
12
9
11
1
2
3
4
5
lucite Cherenkov

Fig. 6

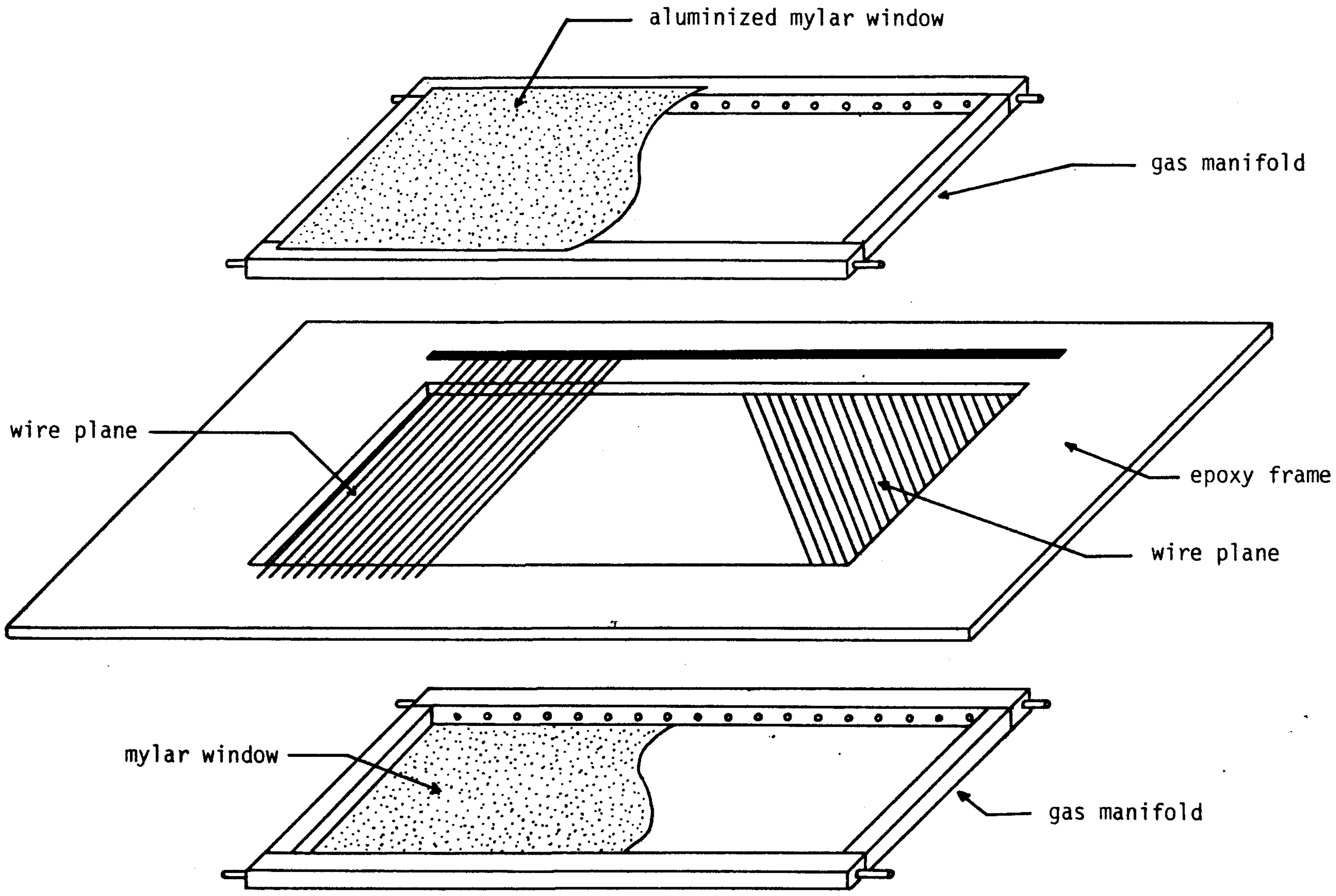
aluminized mylar window
gas manifold
wire plane
epoxy frame
wire plane
mylar window
gas manifold

Fig. 7

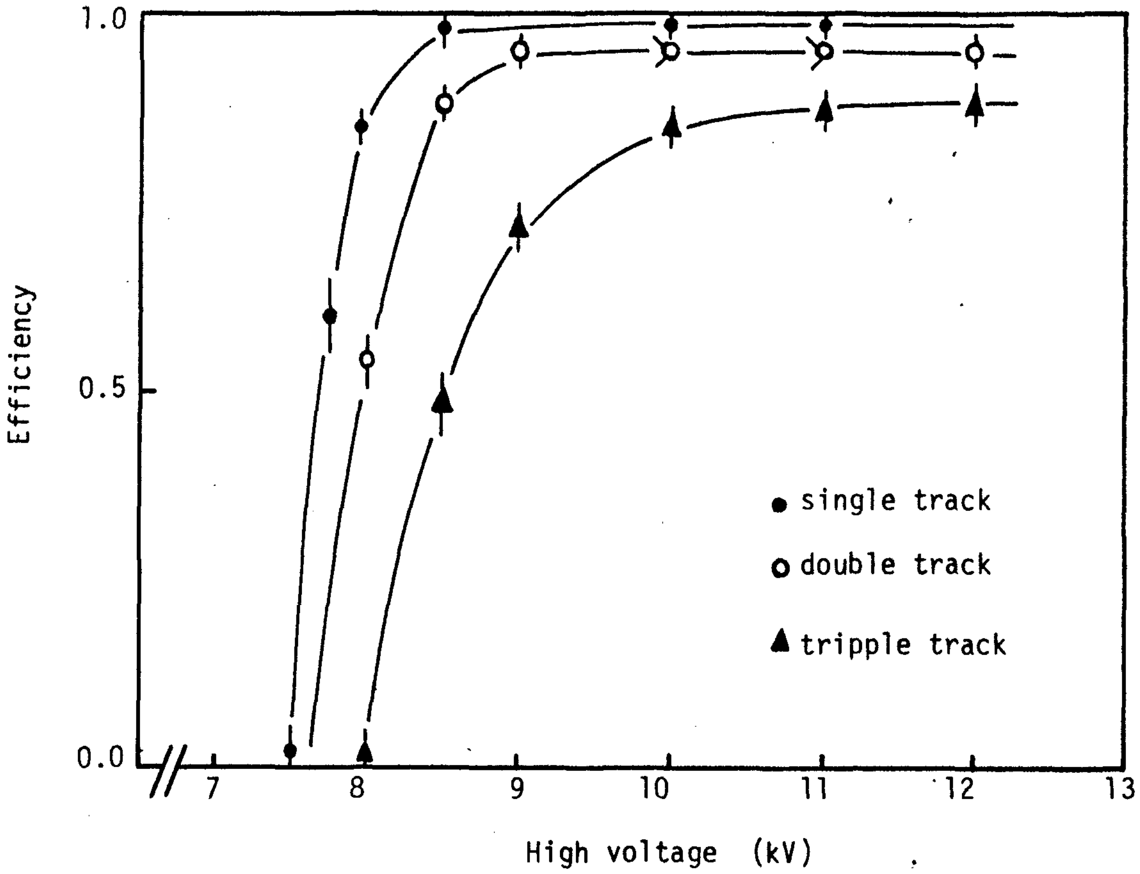
1.0
0.5
0.0
Efficiency
● single track
○ double track
▲ tripple track
7
8
9
10
11
12
13
High voltage (kV)

Fig. 8

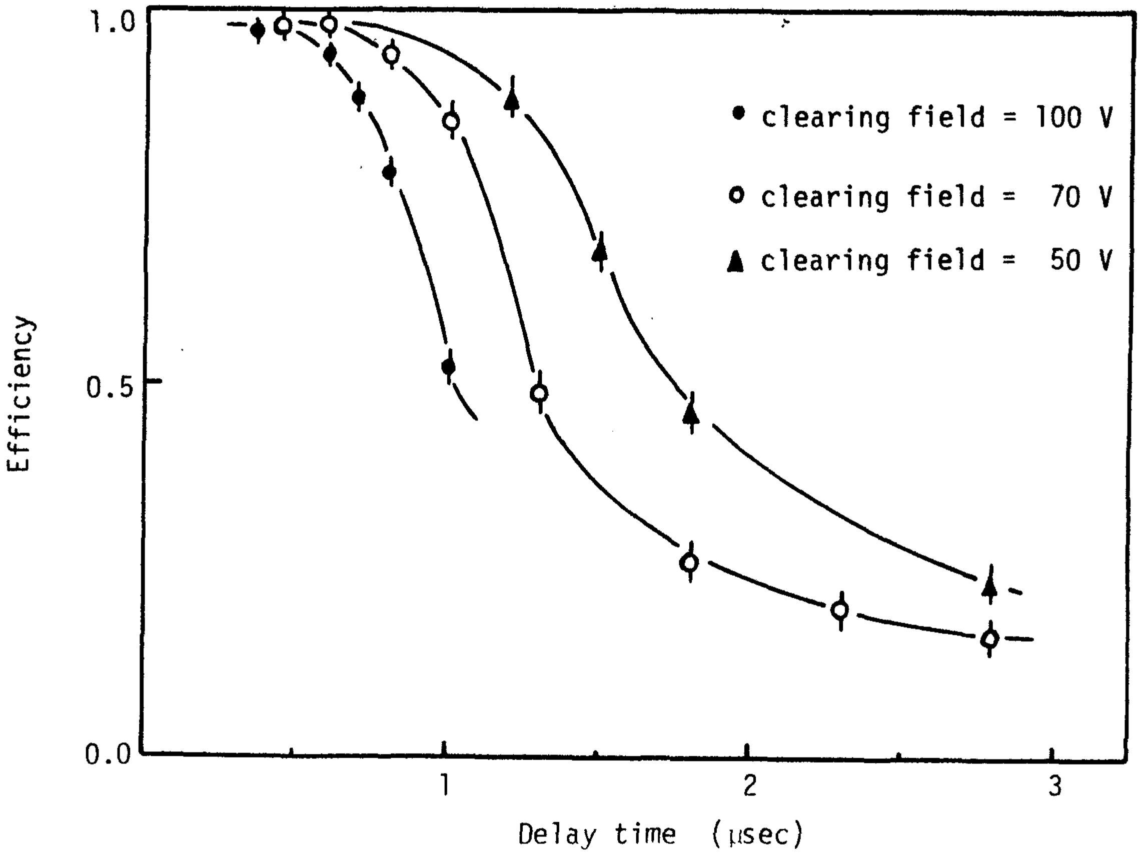
1.0
0.5
0.0
Efficiency
● clearing field = 100 V
○ clearing field = 70 V
▲ clearing field = 50 V
1
2
3
Delay time (μsec)

Fig. 9

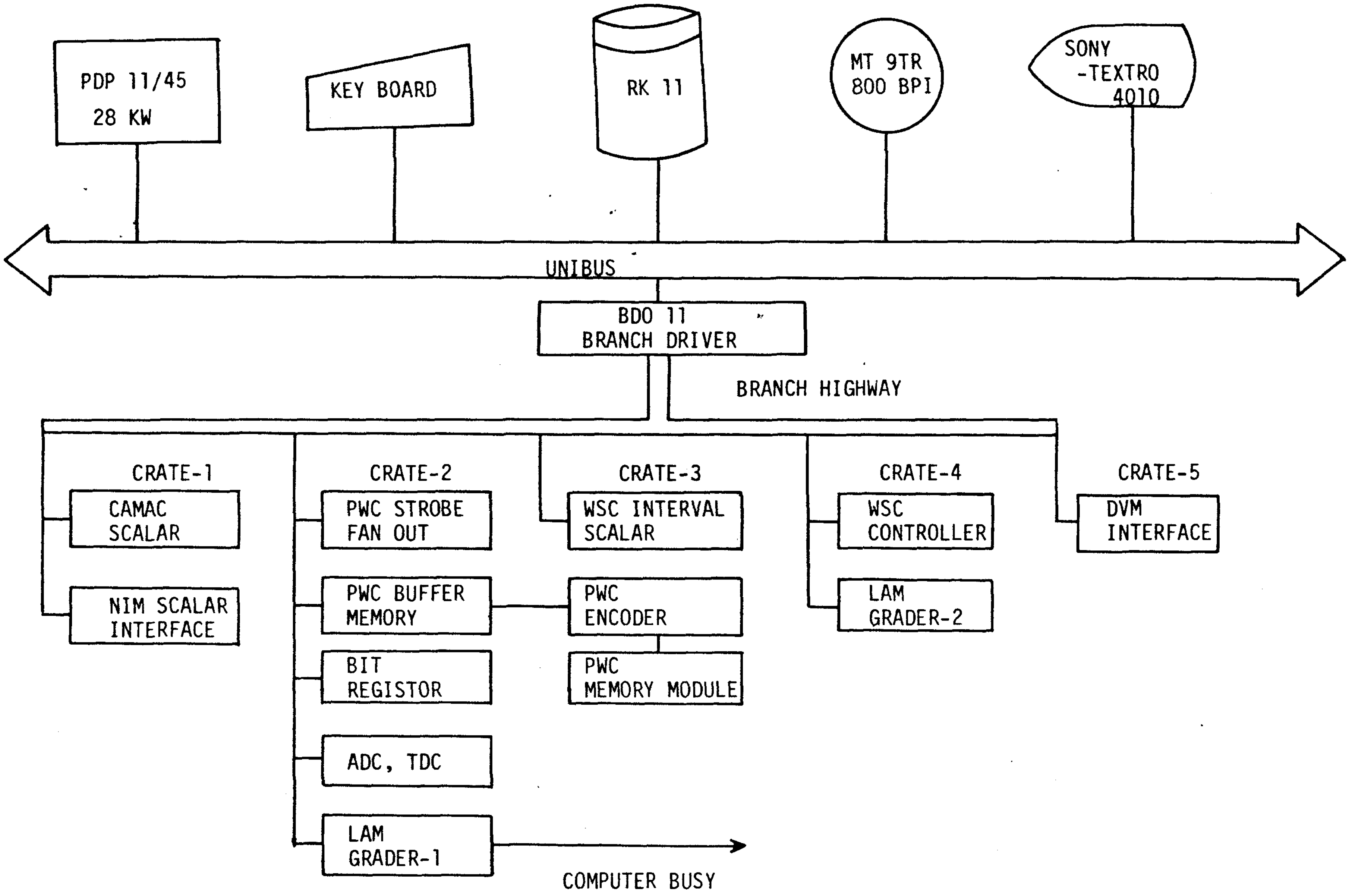
PDP 11/45
28 KW
KEY BOARD
RK 11
MT 9TR
800 BPI
SONY
-TEXTRO
4010
UNIBUS
BDO 11
BRANCH DRIVER
BRANCH HIGHWAY
CRATE-1
CAMAC
SCALAR
NIM SCALAR
INTERFACE
CRATE-2
PWC STROBE
FAN OUT
PWC BUFFER
MEMORY
BIT
REGISTOR
ADC, TDC
LAM
GRADER-1
COMPUTER BUSY
CRATE-3
WSC INTERVAL
SCALAR
PWC
ENCODER
PWC
MEMORY MODULE
CRATE-4
WSC
CONTROLLER
LAM
GRADER-2
CRATE-5
DVM
INTERFACE

Fig. 10

Bit / Word	15	14	13	12	11	10	9	8	7	6	5	4	3	2	1	0
1	Test pattern															
2	Trigger logic															
3					T2 bit									T1 bit		
4				T3 bit												
5					T5 bit											
6												LC bit				
7						(Beam hodoscope X1)										
8						(" Y1)										
9						(" X2)										
10						(" Y2)										
11			Gas Č				Beam momentum hodoscope									
12	Test pattern															
13 / 24	ADC T5-1 ∿ T5-12															
25 / 36	ADC LC-1 ∿ LC-10, Gas Č															
37 / 60	TDC T3-2 ∿ T3-13, T5-1 ∿ T5-12															
61 / 204	WSC Interval Scaler C1 ∿ C6															
205	DMA marker															
206	MWPC data no.															
207 / 256	MWPC data (variable length)															

Fig. 11

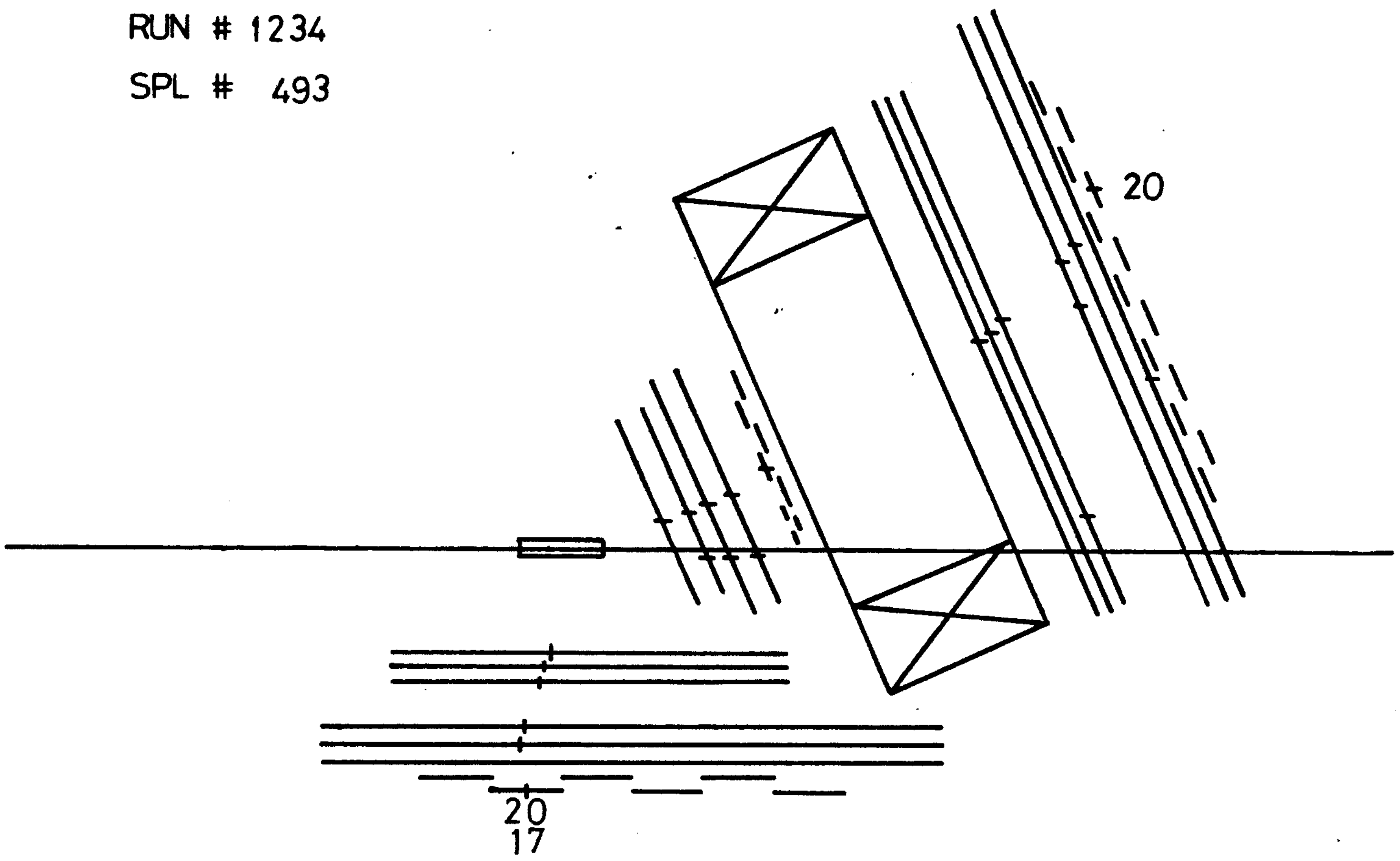

Fig. 12

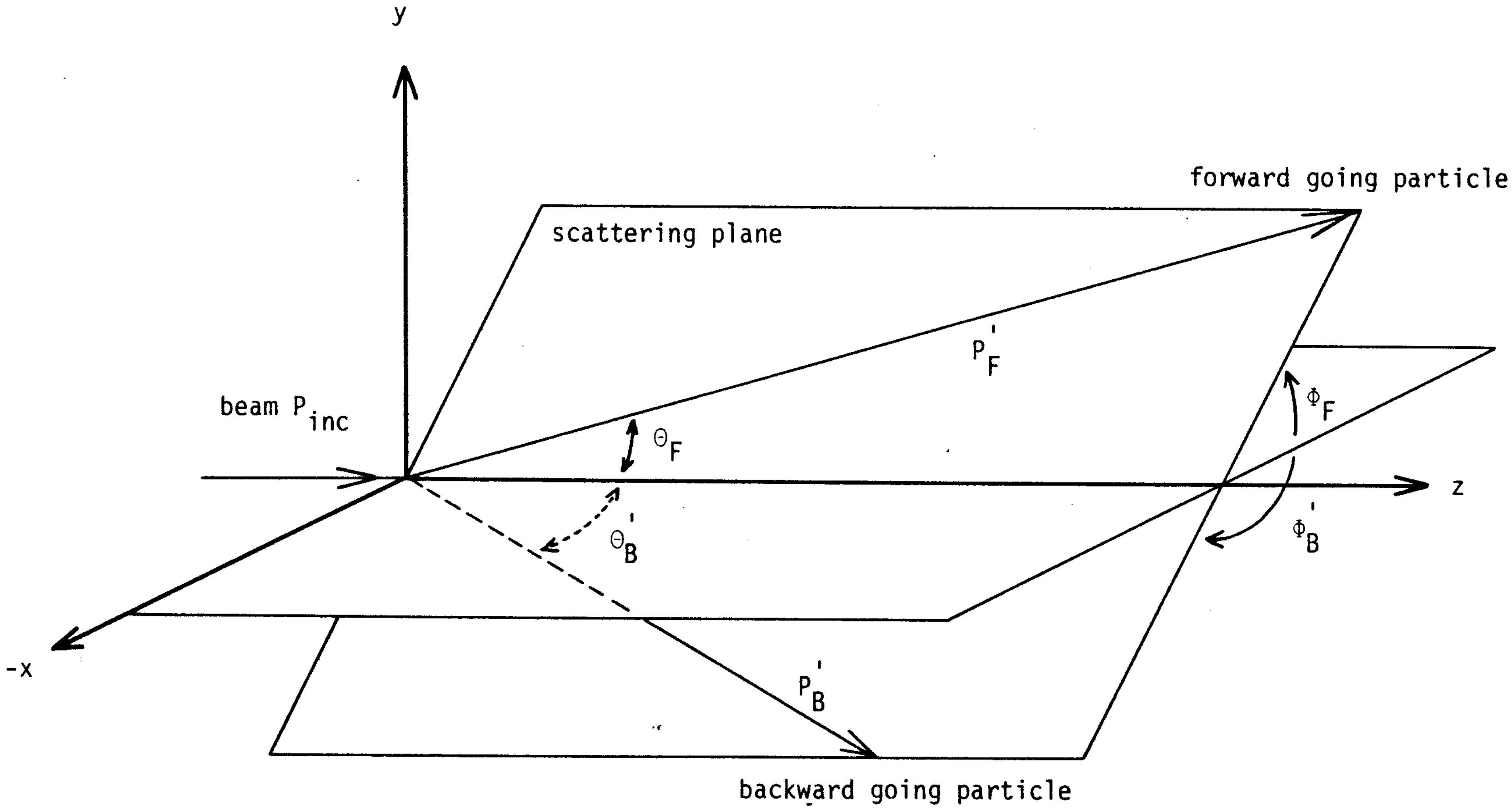
y
forward going particle
scattering plane
P'F
beam Pinc
ΘF
ΦF
z
Θ'B
Φ'B
-x
P'B
backward going particle

Fig. 13

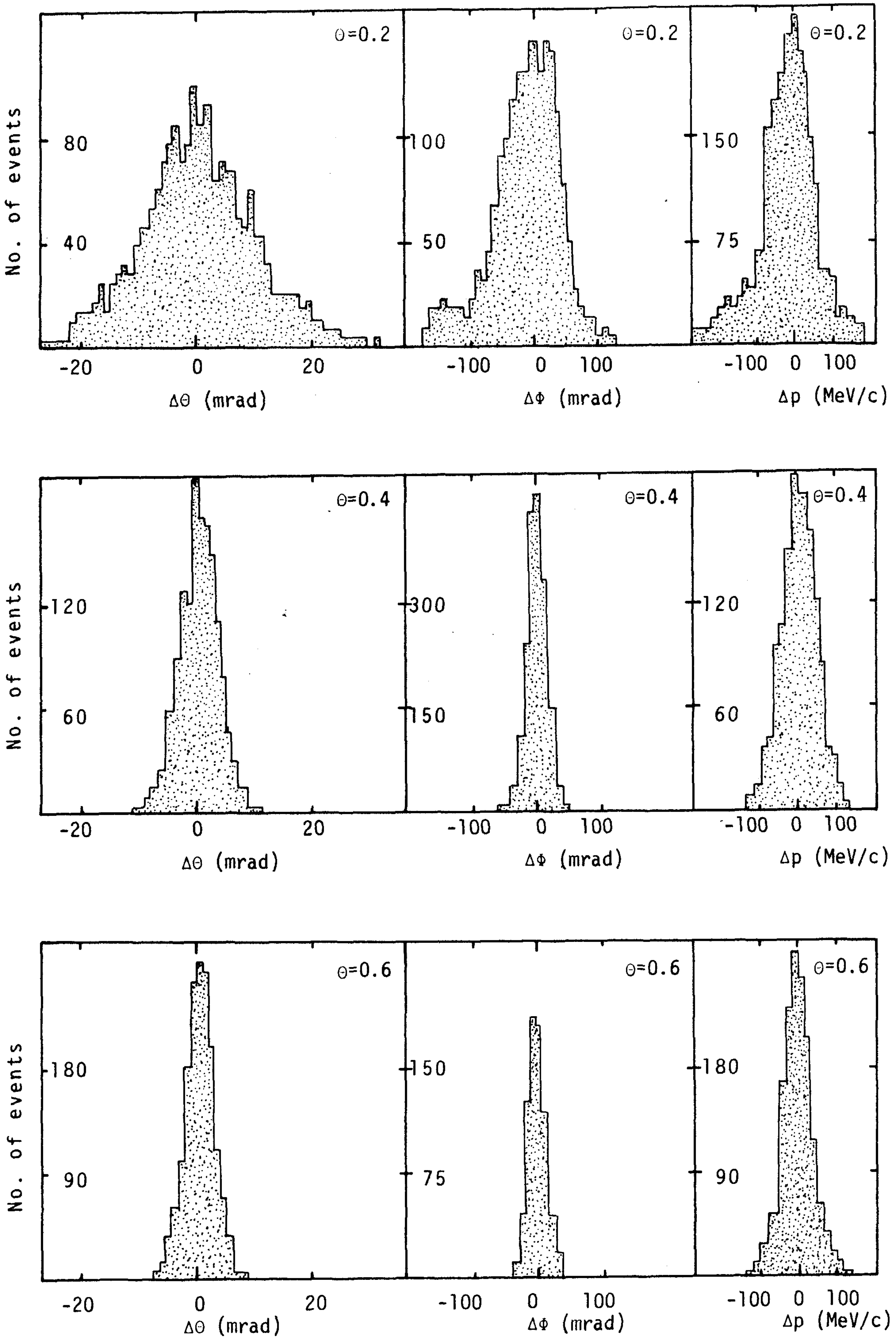
No. of events
θ=0.2
80
40
-20
0
20
Δθ (mrad)
θ=0.2
100
50
-100
0
100
ΔΦ (mrad)
θ=0.2
150
75
-100
0
100
Δp (MeV/c)
No. of events
θ=0.4
120
60
-20
0
20
Δθ (mrad)
θ=0.4
300
150
-100
0
100
ΔΦ (mrad)
θ=0.4
120
60
-100
0
100
Δp (MeV/c)
No. of events
θ=0.6
180
90
-20
0
20
Δθ (mrad)
θ=0.6
150
75
-100
0
100
ΔΦ (mrad)
θ=0.6
180
90
-100
0
100
Δp (MeV/c)

Fig. 14

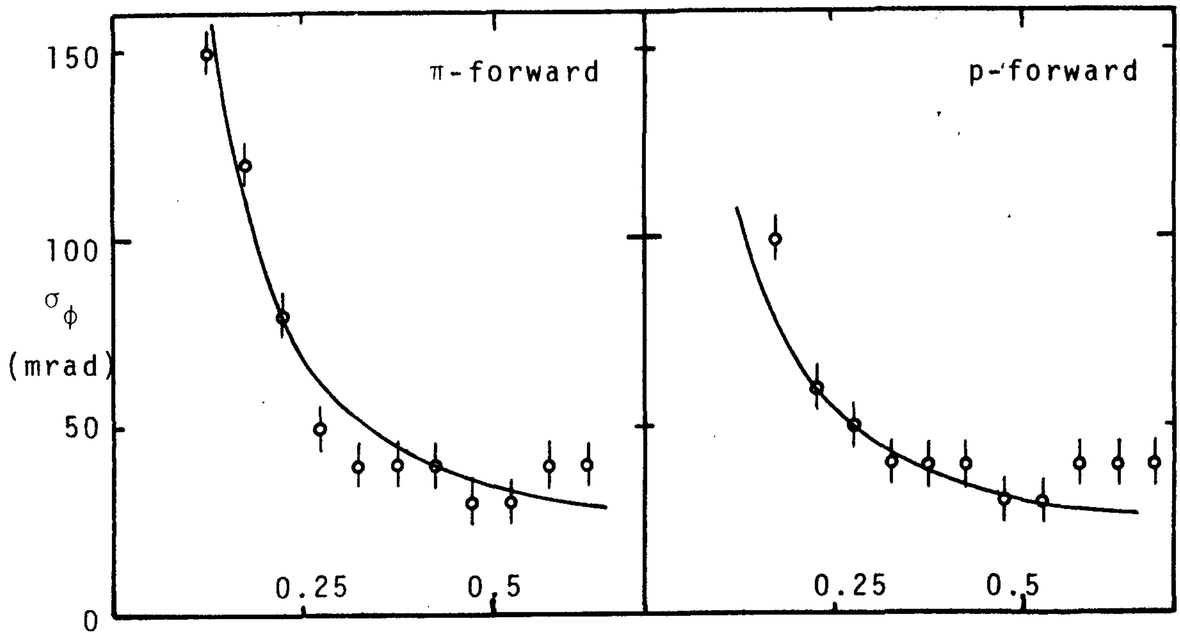

Fig. 15

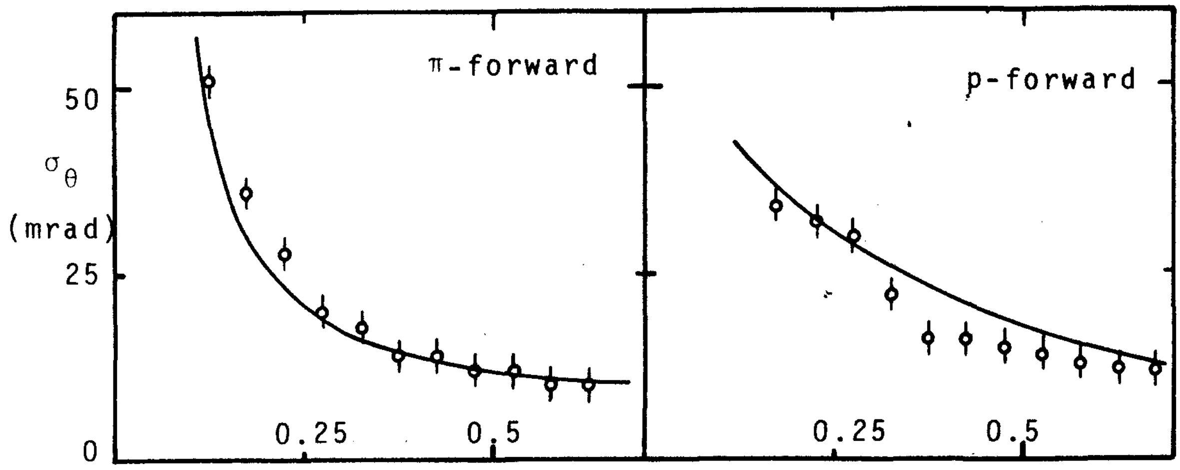

Fig. 16

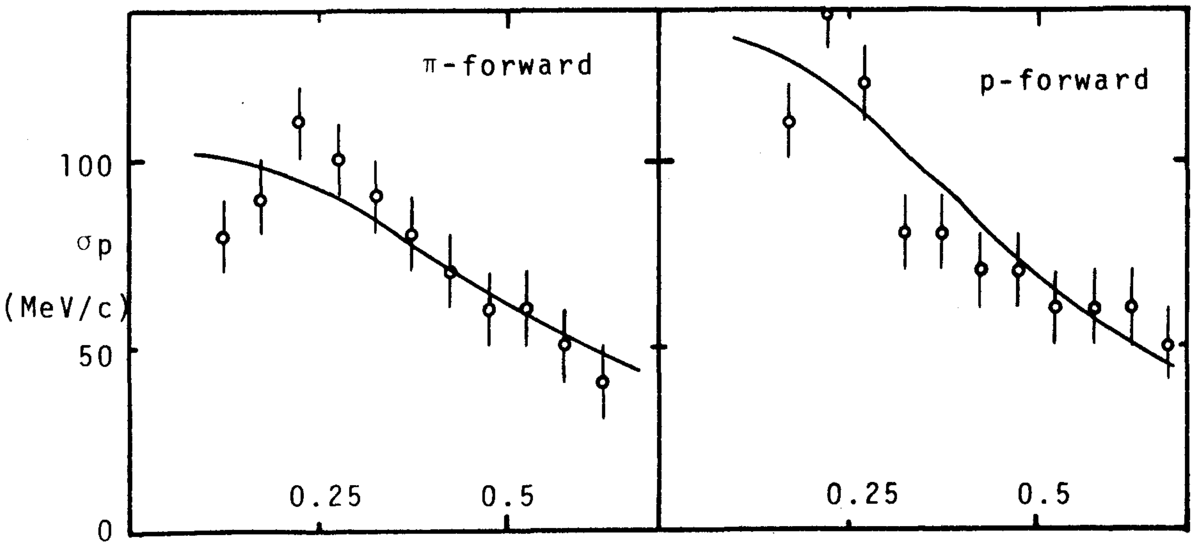

Fig. 17

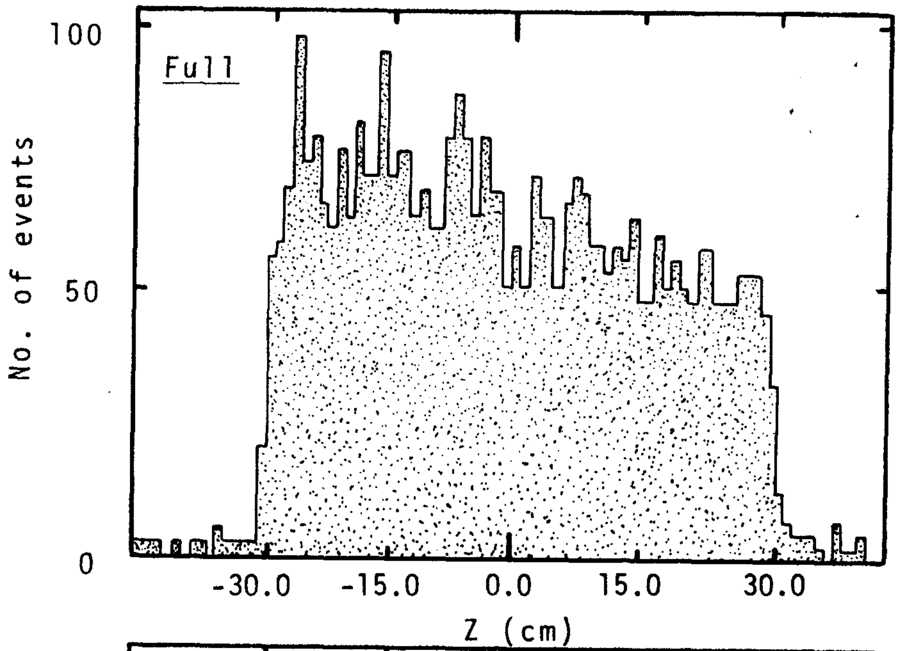

Fig. 18a

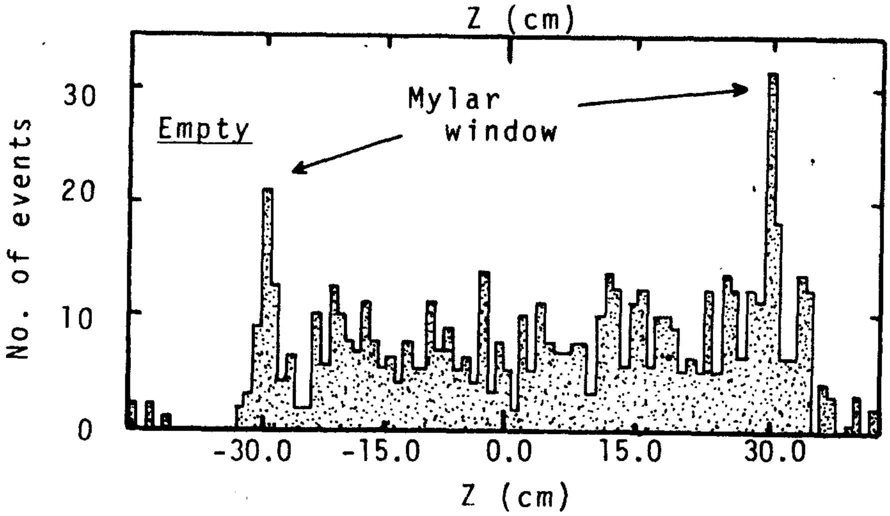

Fig. 18b

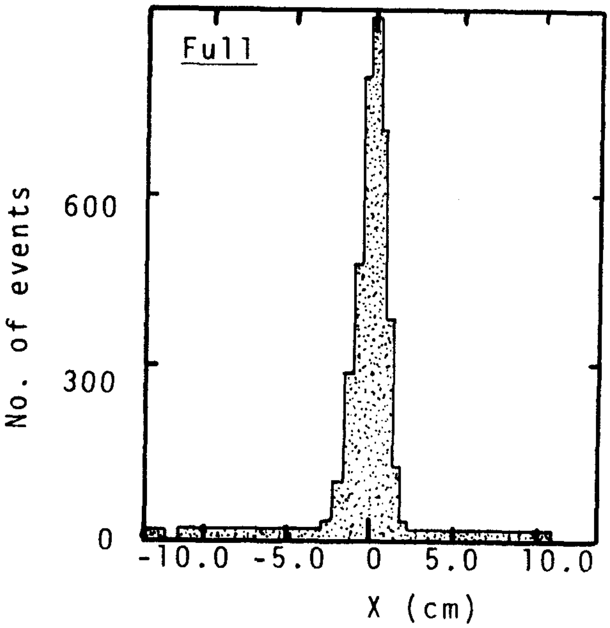

Fig. 19

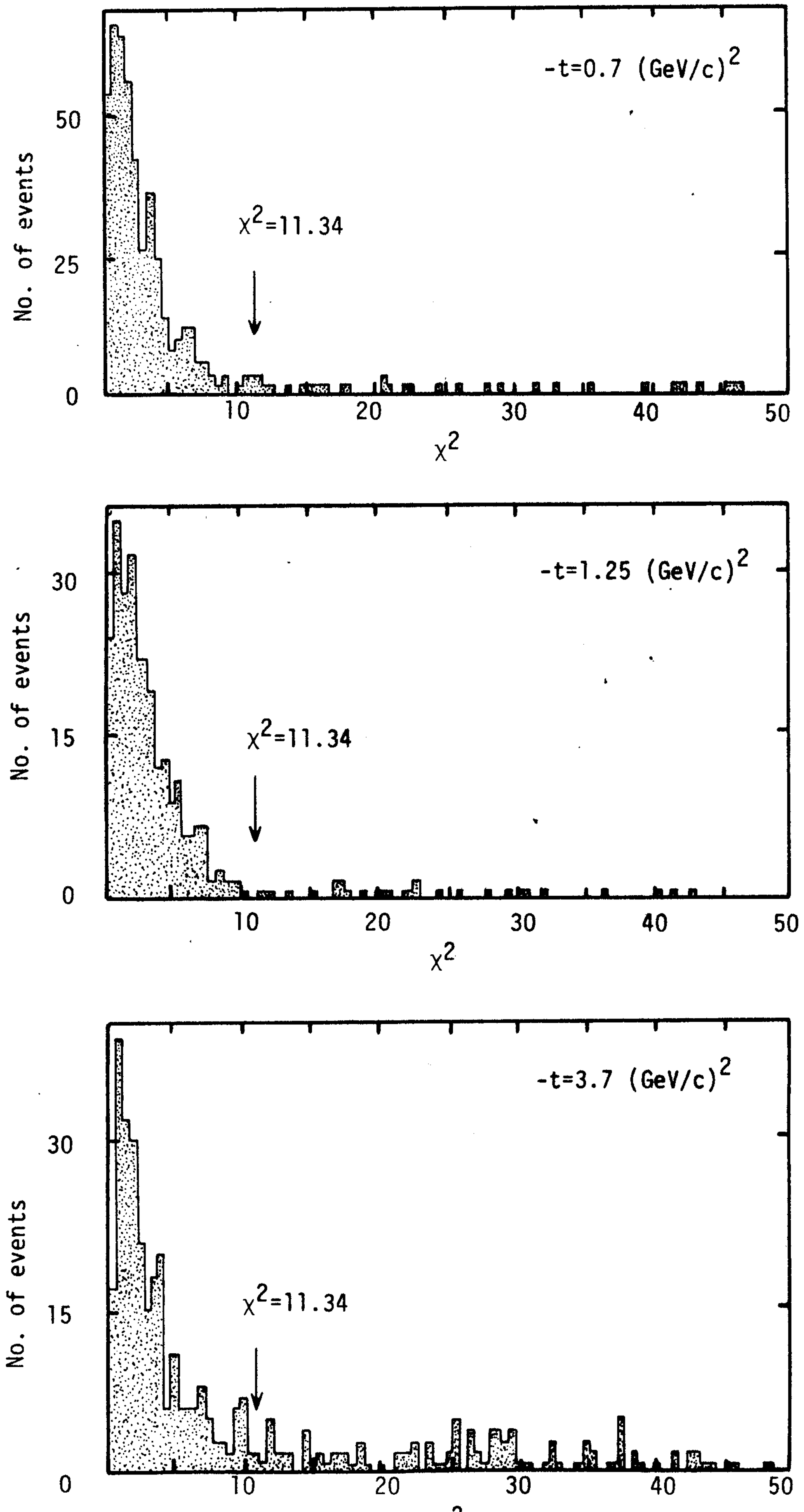
-t=0.7 (GeV/c)^2
No. of events
0
25
50
χ^2=11.34
10
20
30
40
50
χ^2
-t=1.25 (GeV/c)^2
No. of events
0
15
30
χ^2=11.34
10
20
30
40
50
χ^2
-t=3.7 (GeV/c)^2
No. of events
0
15
30
χ^2=11.34
10
20
30
40
50
χ^2

Fig. 20

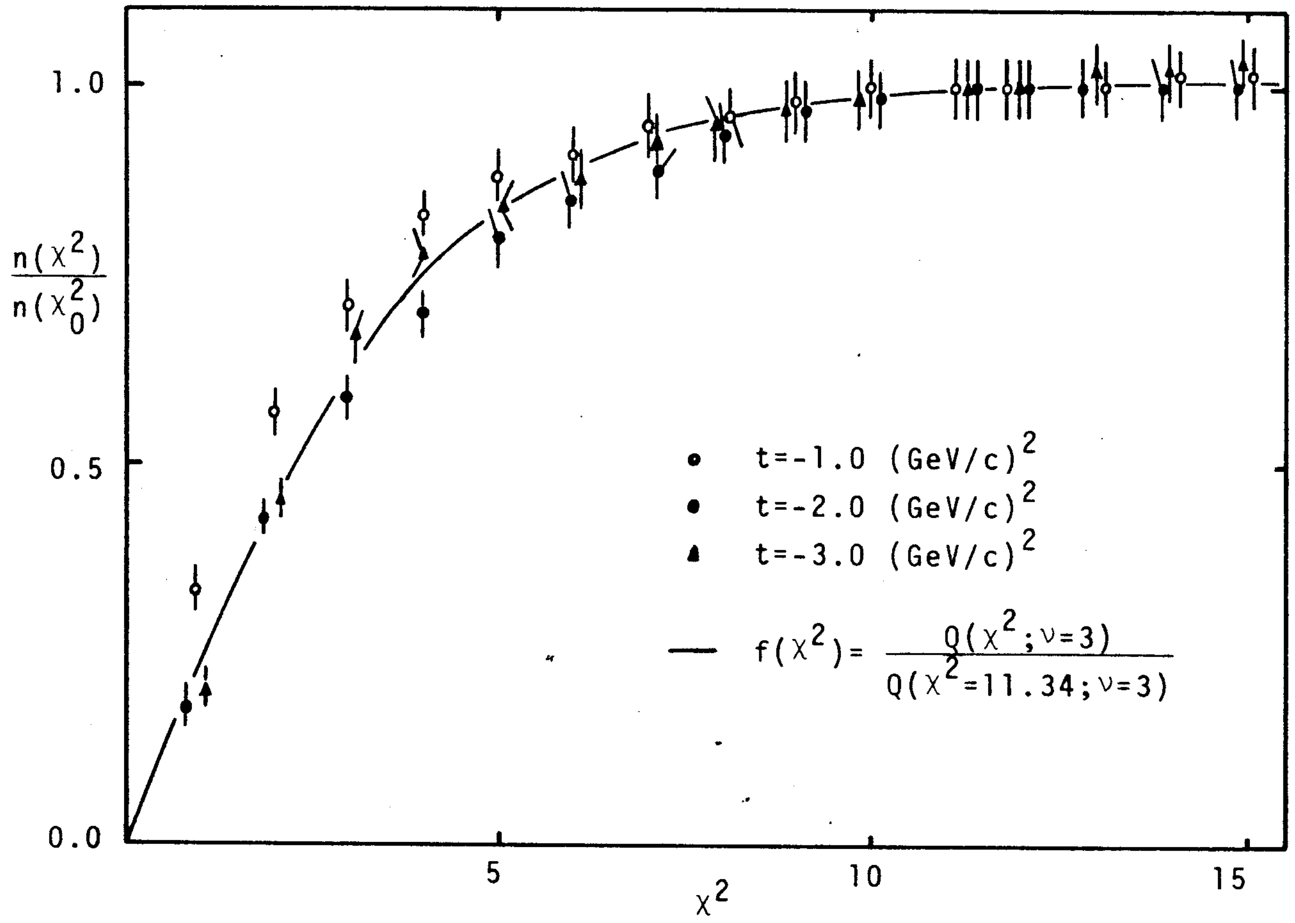
1.0
0.5
0.0
$\frac{n(\chi^2)}{n(\chi_0^2)}$
5
10
15
χ^2
t=-1.0 (GeV/c)^2
t=-2.0 (GeV/c)^2
t=-3.0 (GeV/c)^2
$f(\chi^2) = \frac{Q(\chi^2;\nu=3)}{Q(\chi^2=11.34;\nu=3)}$

Fig. 21

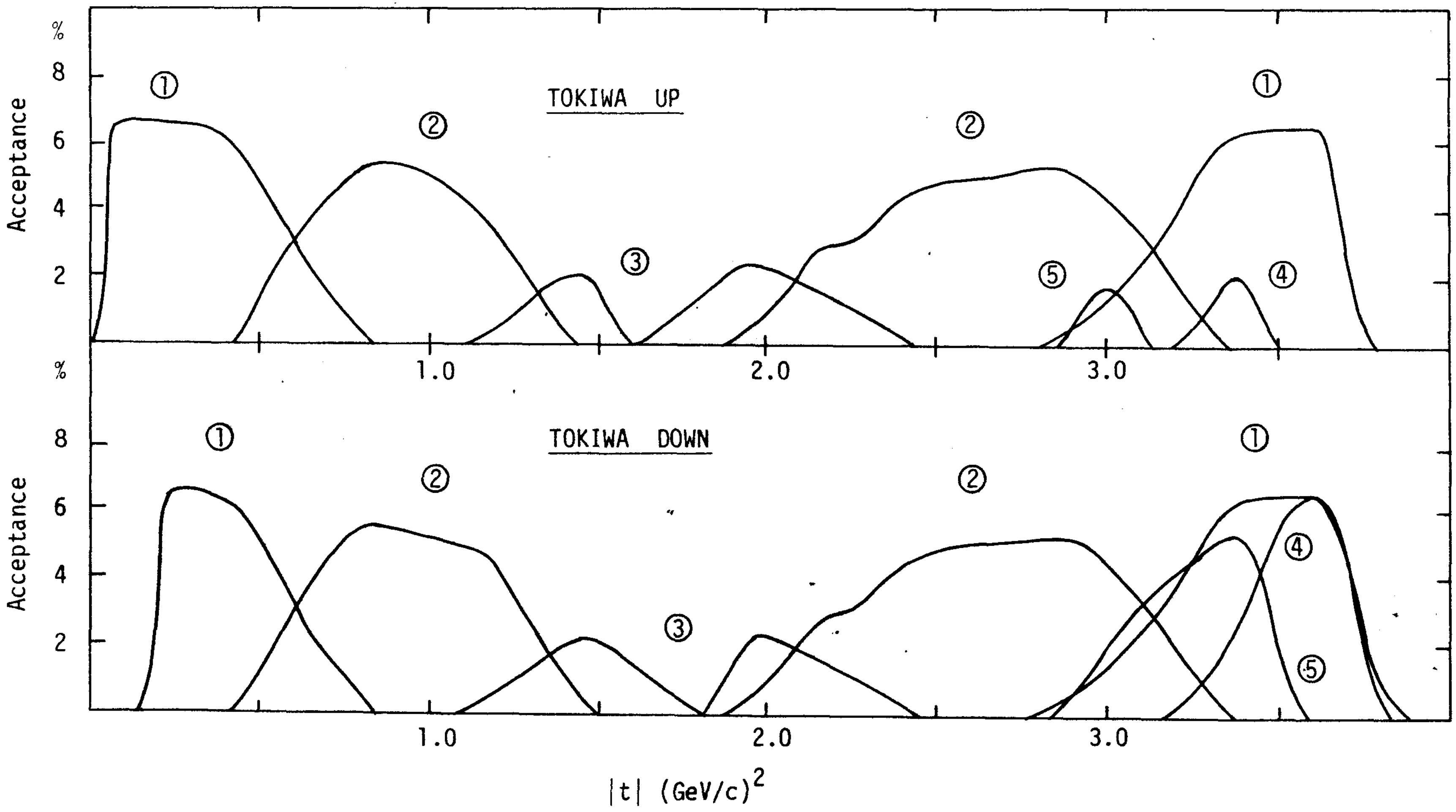
%
8
6
4
2
Acceptance
①
②
TOKIWA UP
③
②
⑤
①
④
1.0
2.0
3.0
%
8
6
4
2
Acceptance
①
②
TOKIWA DOWN
③
②
①
④
⑤
1.0
2.0
3.0
|t| (GeV/c)^2

Fig. 22

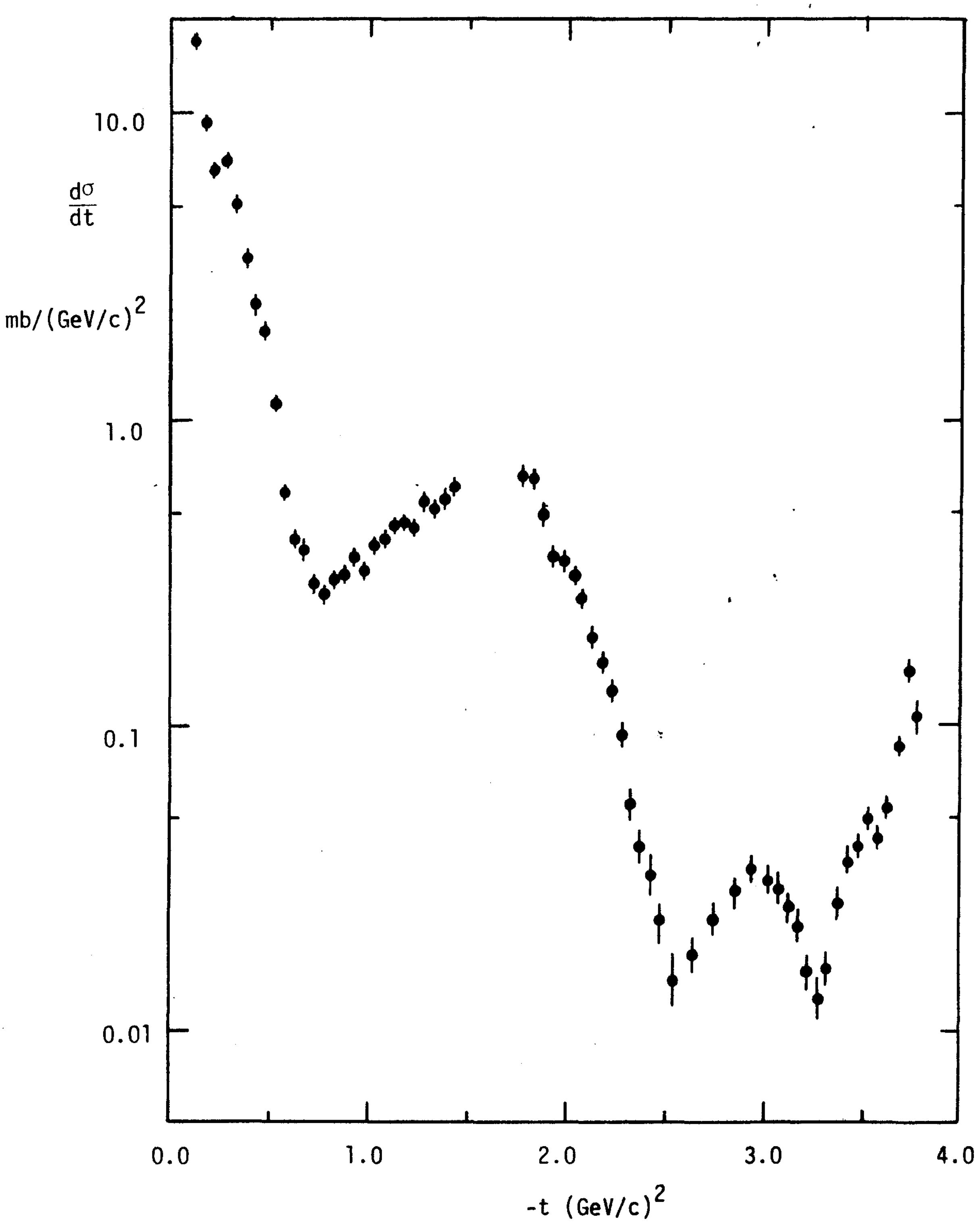

Fig. 23

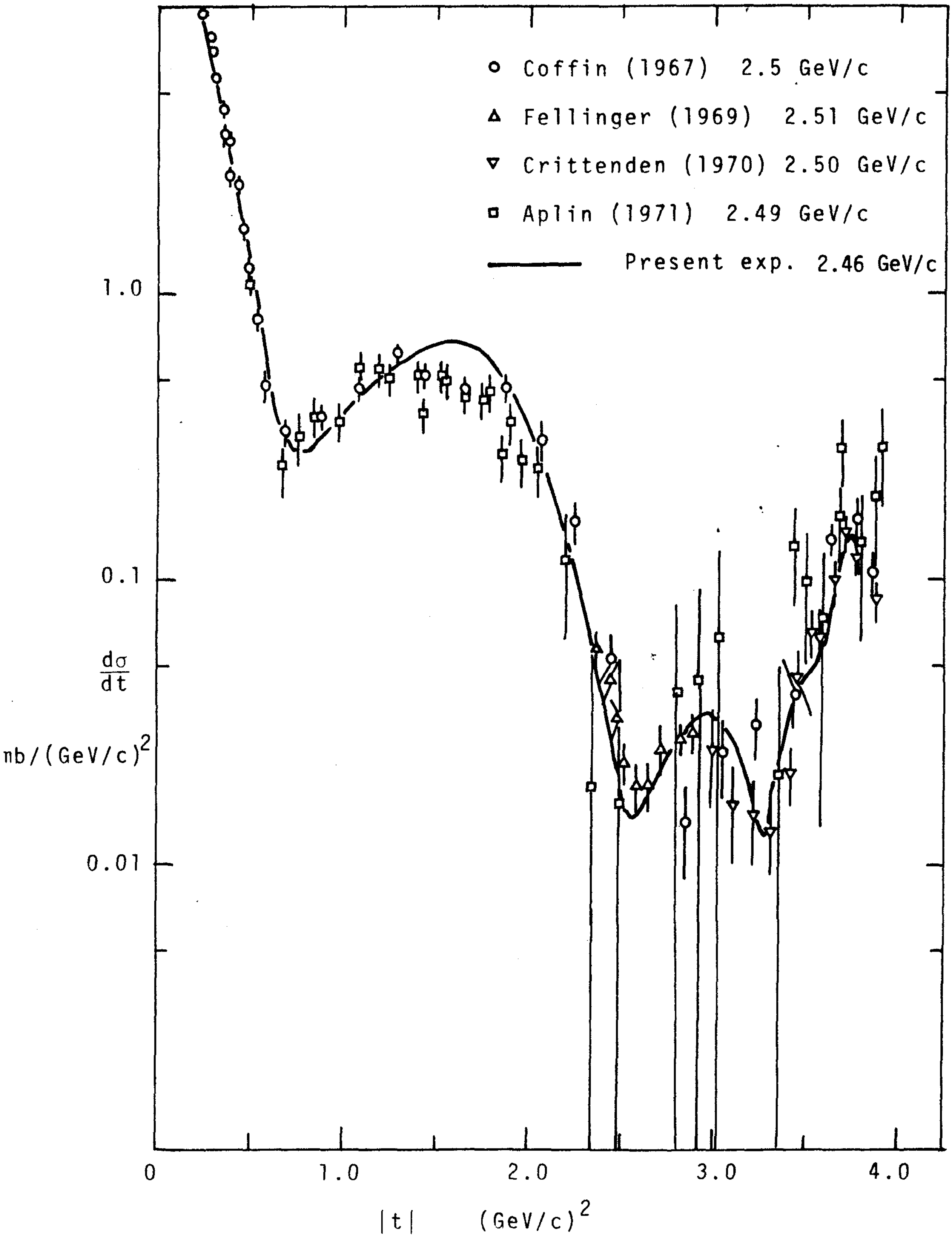
○ Coffin (1967) 2.5 GeV/c
△ Fellinger (1969) 2.51 GeV/c
▽ Crittenden (1970) 2.50 GeV/c
□ Aplin (1971) 2.49 GeV/c
Present exp. 2.46 GeV/c
1.0
0.1
0.01
dσ/dt
mb/(GeV/c)²
0
1.0
2.0
3.0
4.0
|t| (GeV/c)²

Fig. 24

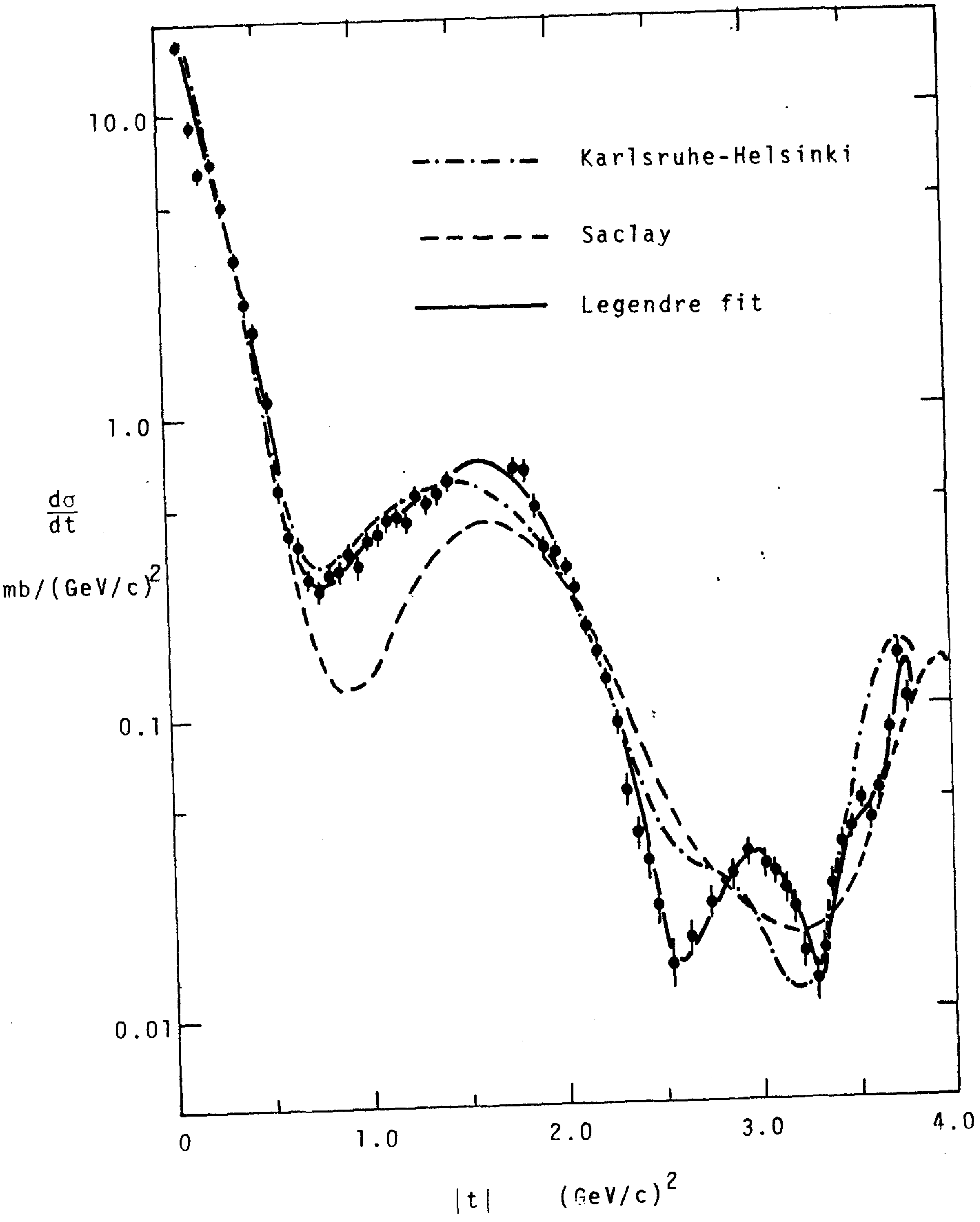
Karlsruhe-Helsinki
Saclay
Legendre fit
10.0
1.0
0.1
0.01
$\frac{d\sigma}{dt}$
mb/(GeV/c)^2
0
1.0
2.0
3.0
4.0
|t| (GeV/c)^2

Fig. 25

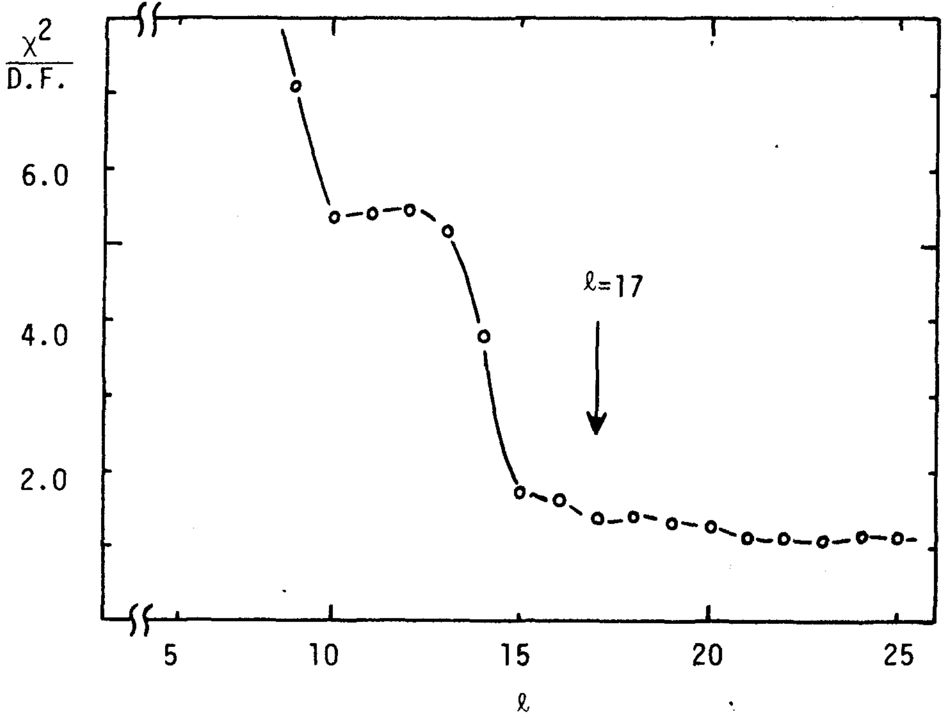
$\frac{\chi^2}{D.F.}$
6.0
4.0
2.0
ℓ=17
5
10
15
20
25
ℓ

Fig. 26

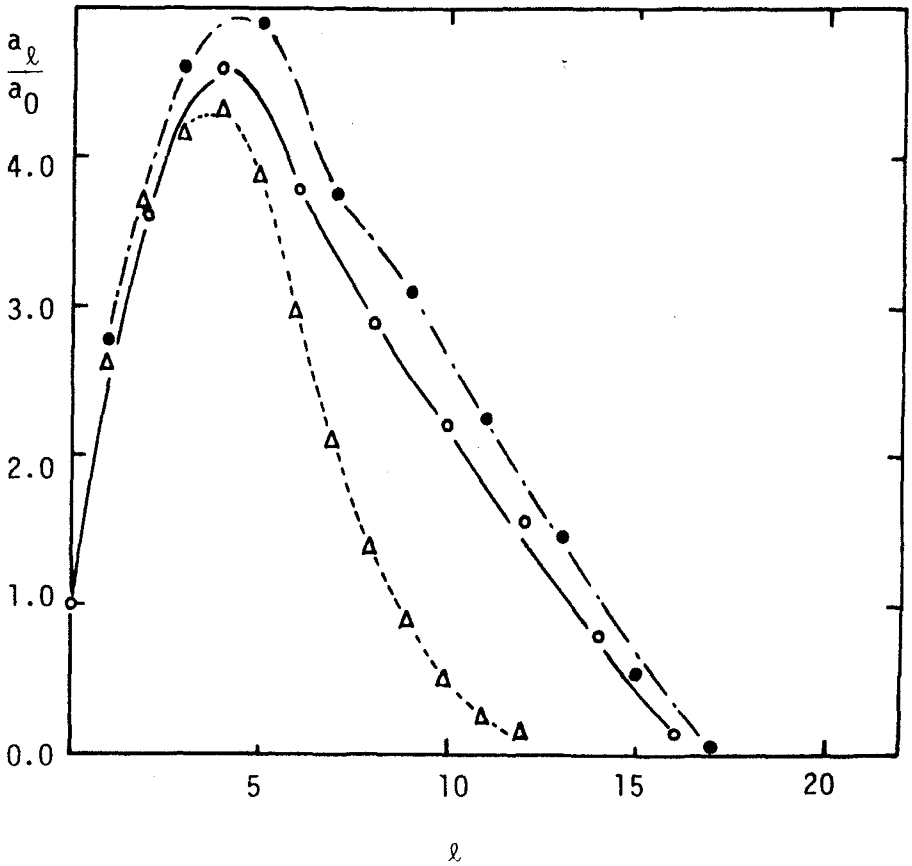
$\frac{a_\ell}{a_0}$
4.0
3.0
2.0
1.0
0.0
5
10
15
20
ℓ

Fig. 27

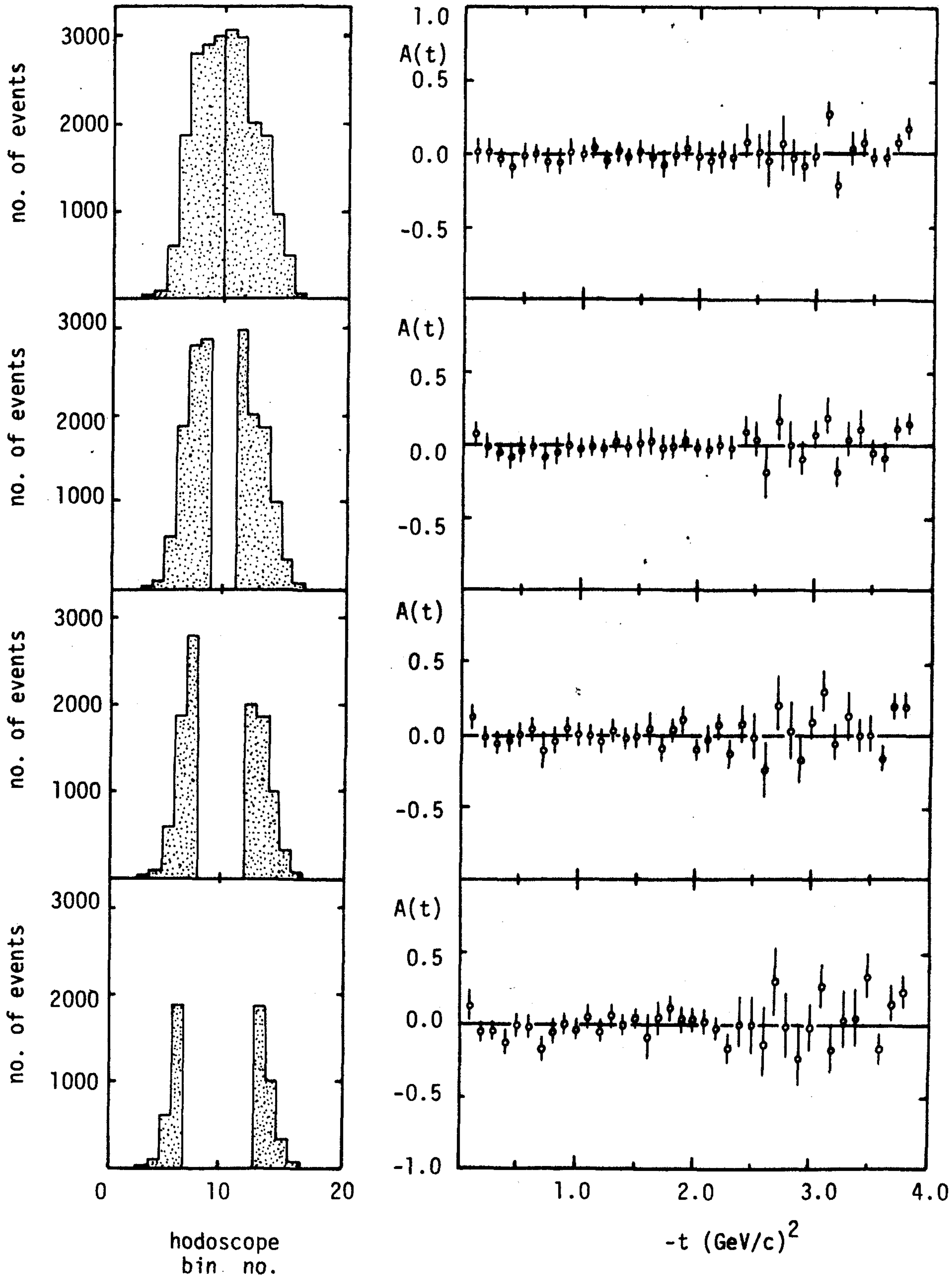
no. of events
3000
2000
1000
0
10
20
hodoscope bin no.
A(t)
1.0
0.5
0.0
-0.5
-1.0
1.0
2.0
3.0
4.0
-t (GeV/c)^2

Fig. 28